remote sensing

MDPI

Article

Joint Characterization of Sentinel-2 Reflectance: Insights from Manifold Learning

Daniel Sousa[1,*] and Christopher Small[2]

Citation: Lastname, F.; Lastname, F.; Lastname, F. Title. *Remote Sens.* **2022**, *14*, x. https://doi.org/10.3390/xxxxx

Academic Editor: Firstname Lastname

Received: date
Accepted: date
Published: date

Publisher's Note: MDPI stays neutral with regard to jurisdictional claims in published maps and institutional affiliations.

[1] Department of Geography, San Diego State University, San Diego, CA, 92182. dan.sousa@sdsu.edu
[2] Lamont Doherty Earth Observatory, Columbia University, Palisades, NY 10964. csmall@columbia.edu
* Correspondence: dan.sousa@sdsu.edu

Abstract: Most applications of multispectral imaging are explicitly or implicitly dependent on the dimensionality and topology of the spectral mixing space. Mixing space characterization refers to the identification of salient properties of the set of pixel reflectance spectra comprising an image (or compilation of images). The underlying premise is that this set of spectra may be described a low dimensional manifold embedded in a high dimensional vector space. Traditional mixing space characterization uses the linear dimensionality reduction offered by Principal Component Analysis to find projections of pixel spectra onto orthogonal linear subspaces, prioritized by variance. Here we consider the potential for recent advances in nonlinear dimensionality reduction (specifically, manifold learning) to contribute additional useful information for multispectral mixing space characterization. We integrate linear and nonlinear methods through a novel method called Joint Characterization (JC). JC is comprised of two components. First, spectral mixture analysis (SMA) linearly projects the high-dimensional reflectance vectors onto a 2D subspace. Second, manifold learning nonlinearly maps the high-dimensional reflectance vectors into a 2D embedding space. The SMA output is physically interpretable in terms of material abundances. The manifold learning output is not generally physically interpretable, but more faithfully captures high dimensional connectivity and clustering. Used together, the strengths of SMA may compensate for the limitations of manifold learning, and vice versa. We illustrate JC using globally standardized Substrate, Vegetation, and Dark (S, V, D) endmembers for SMA, and Uniform Manifold Approximation and Projection (UMAP) for manifold learning, applied to thematic compilations of 90 Sentinel-2 reflectance images selected from a diverse set of global land cover hotspots. The value of each (SVD and UMAP) model is illustrated, both separately and jointly. JC is shown to successfully characterize both continuous gradations (mixing trends) and discrete clusters (land cover class distinctions). These features are not clearly identifiable from

SVD fractions alone, and not physically interpretable from UMAP alone. Implications are discussed for the design of models which can reliably extract and explainably use high-dimensional spectral information in spatially mixed pixels – a principal challenge in optical remote sensing.

Keywords: Joint Characterization; Sentinel-2; Spectral Mixture Analysis; Manifold Learning; UMAP

1. Introduction

The Since the first ERTS-1 images over 50 years ago, Earth scientists have relied on multispectral satellite imaging as a source of impartial, systematic, quantitative observations of land surface processes [1]. These data have advanced in quantity and quality over the decades, enabled by advances in sensor and platform engineering, as well as increasing recognition of the potential value of such data for public and private sectors alike [2,3]. Such advances can be broadly understood as falling along three main axes: increasing spatial resolution, shortening revisit time, and increasing spectral fidelity, e.g. [4,5].

For decades, the Landsat program was the only scientifically available source of decameter scale satellite imagery [6]. Recently, the European Space Agency complemented this public record with the 2015 and 2017 launches of the Sentinel-2A/B constellation [7]. These data fundamentally advance the data record available to Earth scientists along all three axes – increasing spatial resolution to 10 m (20 m for NIR & SWIR bands), shortening revisit to 3-5 days, and increasing the number of spectral bands to 13 (with 11 useful for surface processes).

Multispectral image analysis capabilities have advanced alongside observations. Statistical methods for exploiting high dimensional data have become particularly popular in recent decades, largely referred to by the moniker "machine learning" [8–11]. But while these methods can generate accurate predictions for many problems, such methods are generally limited by their lack of explicit physical basis [12]. Interpretability – scientific understanding of why a given model works, and when it might not work – is thus paramount if these methods are to reach their full potential [13].

One subset of machine learning algorithms, referred to as manifold learning, is designed to preserve high-dimensional connectivity structure (topology) of high dimensional datasets [14,15]. These algorithms are particularly promising in the context of dimensionality reduction – finding an effective, parsimonious representation of the signals of interest present in high dimensional data. In this context, manifold learning can be considered a nonlinear complement [16] to the longstanding linear dimensionality reduction offered by Principal Component Analysis [17]. Dimensionality reduction can be considered an integral subset of the broader question of characterization in the context of a characterization + modeling framework [18]. Decameter scale multispectral imagery in particular may provide particularly well-connected high-dimensional topologies due to the prevalence of spatial autocorrelation [19] and efficacy of spectral mixture models [20–22].[23][24][25][26][27]

Recently, the potential to exploit synergies between complementary dimensionality reduction methods has been used to perform joint characterization (JC). Briefly, joint characterization uses the strengths of one dimensionality reduction algorithm to mitigate limitations of another algorithm. This has been shown effective for synthetic images [28], airborne hyperspectral data [28,29], multispectral image time series [30], and gridded climate data [31]. But to our knowledge, no comparative analysis has yet been performed in which joint characterization is applied systematically to globally diverse compilations of image spectra across a broad range of land cover types.

Here we conduct such an analysis. Specifically, we illustrate the joint characterization approach for a globally diverse compilation of 90 Sentinel-2 image subsets representative of 9 globally prevalent land cover classes. We implement joint characterization of the composite spectral mixing space using a globally standardized Substrate, Vegetation, Dark (S,V,D) spectral mixture model [32] as our physical characterization, and the Uniform Manifold Approximation and Projection (UMAP) [33] as our topology-preserving manifold learning algorithm. In so doing, we ask the following questions:

1. *Geophysical*
    a. What is the overall S,V,D fraction distribution of globally diverse representatives of significant land cover classes?
    b. How well does the global S,V,D model fit each land cover class, as measured by root mean square misfit?

2. *Topological*
    a. How clustered or continuous are the manifolds for each land cover category found by UMAP?

3. *Joint*
    a. To what extent can S,V,D fractions and UMAP clusters be used together to yield useful information? Specifically,
        i. To what extent are UMAP clusters geographically contiguous?
        ii. To what extent do disparate UMAP clusters at similar S,V,D fraction values represent physically plausible and/or spectroscopically interpretable spectral variability?
        iii. Are some S,V,D fractions, or land cover classes, better suited to JC than others? If so, why? If not, why not?

references.

2. Materials and Methods

2.1. Data

110 Sentinel-2 image tiles were acquired as Level 1C exoatmospheric reflectance from the USGS EarthExplorer data portal (https://earthexplorer.usgs.gov/). Sites were selected to span a broad geographic diversity, sampling all major biomes and a wide range of geologic histories (Figure 1).

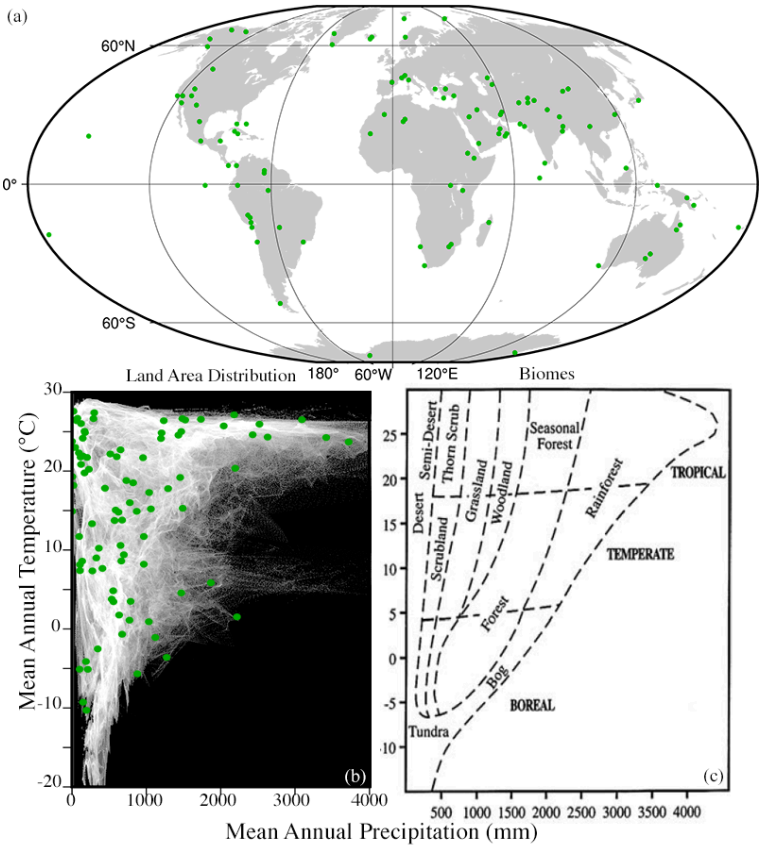

Figure 1. Geographic and climatic distributions of 110 Sentinel-2 tiles from spectral diversity hotspots. Geographic distribution of sample sites is guided by climatic and geologic diversity as well as overall species biodiversity. Individual tile selection criteria favor spectral diversity arising from land cover diversity within and across biomes. Tile geographic coverage corresponds well to global land area distribution within the climatic parameter space (lower left) based on 1 degree monthly mean temperature and precipitation (1900-2002) from [34]Mitchell and Jones (2005). All biomes are well represented. Biome classification (lower right) adapted from [35]Houghton et al. (1996).

90 subsets were selected as representatives of dominant land cover classes. Each subset covered a 10 x 10 km (1000 x 1000 pixel) area dominated by a particular land cover class. The classes used were: agriculture, sand, lava/ash, urban, forest, senescent vegetation, tundra, wetland/mangrove, rock, and alluvium. For the agriculture, sand, wetland, rock, and alluvium classes, 10 representative subsets of each were used. For the lava/ash, urban, senescent vegetation, and tundra classes, 5 subsets of each were used. For the forest class, 20 subsets were used and subsequent analysis was decomposed into two 10-tile portions. The full mosaic is shown in Figure 2 as a SWIR/NIR/Visible false color composite. Scene IDs for each subset are listed in a Supplementary Table.

[32]

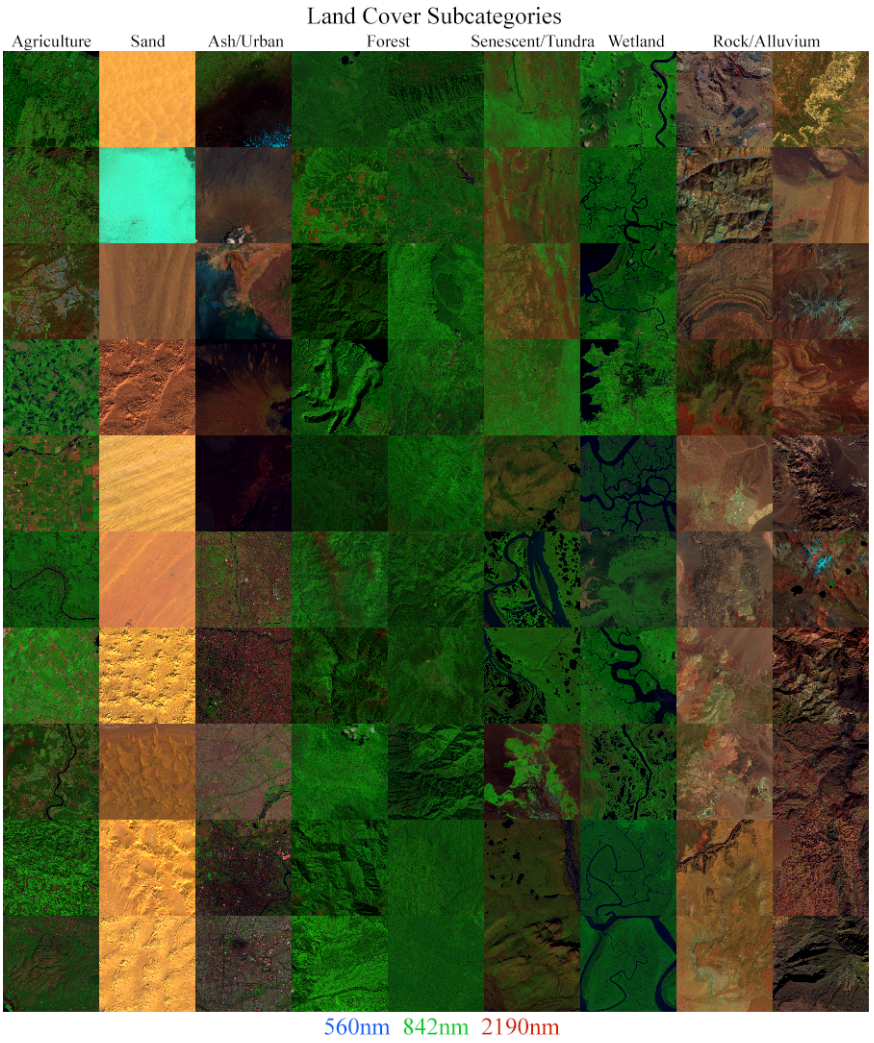

Figure 2. Sentinel-2 composites for land cover subcategories (10 x 10 km) selected from individual hotspot tiles. 1% linear stretch applied.

2.2. Methods

The joint characterization workflow proceeded with the following three steps:

A. Use a linear spectral mixture model to characterize the overall S,V,D distribution of each land cover class (*variance-based, physical, linear*).
B. Use Uniform Manifold Approximation and Projection (UMAP; [33]) to characterize interdimensional topology & clustering (*topology-based, statistical, nonlinear*)
C. Synthesize Steps A and B into a set of 1 or more bivariate distributions which use the physical meaning of the Step A fraction distributions to differentiate among purely topological relations identified from Step B (*joint characterization*).

Spectral signatures of clusters identified from Step C were identified, region of interest (ROI) means and spectral separability metrics were computed, and geographic coherence was visually evaluated.

Each step is explained briefly below.

3.1.1. Step A: Linear Characterization and Modeling: Spectral Mixture Analysis

For the linear component of this analysis, the spectral feature space of the 90-tile mosaic was characterized using Principal Component Analysis [17] (Figure 3, left) as described by [32]Small and Sousa (2022). Consistent with numerous studies with other multispectral and hyperspectral sensors [36–41], the preponderance of variance was were found to be well-characterized by a small number of dimensions (95% of variance in the first 2 dimensions; 97% in the first 3 dimensions). Also consistent with previous studies, the low-order spectral feature space of this diverse mosaic was found to be well-represented by linear mixing among Substrate, Vegetation, and Dark (S,V,D) spectrally distinct endmembers. All tiles were then unmixed to S,V,D fractions using the lower amplitude mean (S_I,V_I,D) endmembers [32](*Small and Sousa, 2022*). Bivariate fraction distributions (Figure 3, right) show fraction estimates to be within the physical range (0 to 100%) for all tiles except high albedo sands, which give S_I fractions >100% and D fractions <0. Mixture model misfit, as quantified by the Root Mean Square Error (RMSE) of misfit between observed and modeled spectra, was < 6% for > 99% of spectra. Due to the unit sum constraint, and the fact that the 3D SVD space maps onto a linear 2D subspace, fraction distributions can also be visualized using a barycentric plot (i.e., ternary diagram) with no loss of information. The remainder of this analysis uses such a visualization to demonstrate variability in S,V,D fraction abundance among land cover classes. For greater detail on variance-based characterization of this mosaic, see [32].

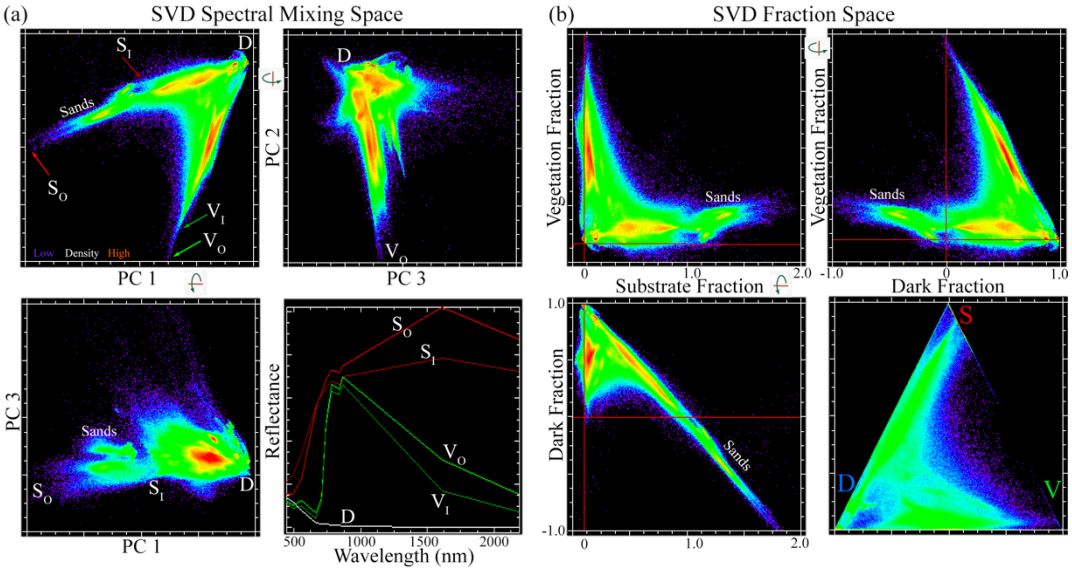

Figure 3. Sentinel-2 SVD spectral mixing space, spectral endmembers, and corresponding SVD fraction space. An eight column (80,000,000 spectra) subset of the Land Cover Subcategory mosaic encompassing the SVD-bounded plane of the full mixing space is effectively 2D with PC dimensions 1 (81%) and 2 (14%) accounting for 95% of total variance, compared to PC 3 (2%). Maximum amplitude (Outer) and lower amplitude mean (Inner) endmember spectra for Substrate and Vegetation define bases for maximal and minimal SVD models (left). Inversion of the minimal model provides liberal estimates of SVD fractions (right) but excludes pure sand landscapes. Because sands lie outside the minimal SVD model, their Substrate fractions exceed 1.0 with Dark fractions < 0. A planar SVD fraction distribution can be projected onto a 2D ternary diagram (lower right) with no loss of information.

[20–22][42][36,43,44]

3.1.2. Step B: Nonlinear Characterization and Modeling: Manifold Learning

In this analysis, nonlinear characterization was based on Uniform Manifold Approximation and Projection (UMAP) [33] of the 11D spectral mixing space. Briefly,

UMAP is a recently developed, increasingly popular algorithm for nonlinear dimensionality reduction. Mathematically, UMAP assumes that the Sentinel-2 spectra are uniformly distributed on a locally connected Riemannian manifold with an (approximately) locally constant Riemannian metric. UMAP models this manifold using a fuzzy topological structure, then seeks a low-dimensional (2 or 3D) embedding with an optimally similar fuzzy topological structure. In general, the resulting embedding is nonlinear and not invertible.

UMAP results depend on choice of several tunable hyperparameters. Among the most important are:

- `n_components` : The number of dimensions in the low-D embedding.
- `n_neighbors` : The size of the local neighborhood used when learning the manifold structure of the data.
- `min_dist` : The limit on how closely spaced points may be spaced in the output space.
- `metric` : The distance metric in the input space of the data.

For all figures in the following analysis, we use the following values:

- `n_components` = 2
- `n_neighbors` = 30
- `min_dist` = 0.1
- `metric` = Euclidean

For the sake of presentation, we defer an illustration of dependence on hyperparameter setting to the Supplement.

All UMAP computations were performed using the open source umap-learn Python package on a commercially available laptop computer with 32 GB RAM, 2GHz Quad-Core Intel Core i5 CPU, and a 1536 MB Intel Iris Plus Graphics GPU. Runtime for the 10 tile (10,000,000 11-band spectra) subsets was 2 hours. For more information about UMAP, see:[45] https://umap-learn.readthedocs.io/en/latest/index.html

3.1.3. Step C: Joint Characterization: Bivariate distributions and Cluster Identification

Linear and nonlinear methods were then combined to perform a joint characterization of the spectral mixing space. In this analysis, we implement JC using bivariate distributions of the linear and nonlinear mixing space characterizations. This step leverages interrelationships between variance-based (spectral mixture fraction) and topology-based (UMAP embedding) metrics.

In the context of this analysis, the mutually reinforcing goals of JC are to: 1) use the mixture fractions to imbue the UMAP embedding with physical meaning, and likewise 2) to use the UMAP embedding to differentiate between subsets of otherwise apparently continuous, indistinct mixture fractions.

Conceptually, JC follows approaches like [46,47] in seeking a robust analytic framework capable of both a) exploiting (potentially) high dimensional and/or nonlinear signals, and b) adhering to the well-known physical constraints of linear mixing processes. The chief novelty is in the fusion of recent developments in manifold learning with a now well-established low-order global S,V,D spectral mixing space.

In the subsequent analysis, spectral endmember fractions are shown on the x-axis and UMAP embedding is shown on the y-axis. Different endmember fractions are more or less useful for understanding different land cover types, so the choice of S, V, or D endmember used in the JC plot(s) is dependent on the land cover subcategory.

3. Results

3.1. Agriculture

Figure 4 illustrates the JC workflow as applied to a compilation of 10 tiles from diverse agricultural basins worldwide. From the SVD ternary diagram (top left), we see that this collection spans nearly the entire global SVD mixing space. These spectra are well-fit by the global mixture model (99% spectra with <5% RMSE). Pixels with fractions near 1.0 are observed for each endmember. Both S:D and D:V binary mixtures are observed. Consistent with previous studies, the edge of the space corresponding to S:V binary mixing is much sparser, as expected due to the ubiquity of subpixel shadow in even the flattest and smoothest natural landscapes.

The 2D UMAP embedding (top center) suggests that most of the geographic area is well-represented by a single broad, well-connected manifold, but several exceptions are also present in the form of both apexes to the main manifold and smaller pixel clusters disconnected from the main manifold. Joint Characterization (bottom row) shows this useful manifold structure can be present at high fractions for all three S,V,D endmembers. ROI mean spectra with high S endmember fractions show plausible differences in soil moisture, albedo, and/or composition. Dominant variability in JC-identified V endmembers corresponds predominantly to SWIR1 (suggestive of leaf water) and visible bands (suggestive of differences in pigments). Variability in JC-identified D endmembers largely corresponds to overall brightness in the NIR and SWIR (turbidity/flotsam?) and curvature in the visible (chlorophyll, CDOM?).

All endmembers were identified as ROIs from the JC plots. These ROIs were then back-projected onto both the ternary diagram and UMAP plot, and visualized in geographic space for 1 example tile from the 10 comprising this land cover compilation (top right). Geographic coherence (e.g., spatial clusters conforming to visually distinct intra- and inter-field boundaries) strongly implies that the ROIs are likely to have physically meaningful distinctions. Examination of the back-projected ROIs on the ternary diagram shows that they would clearly not be distinct from examination of S,V,D fractions alone; examination of the ROIs on the UMAP plot shows that they would have no physically interpretable context from UMAP alone.

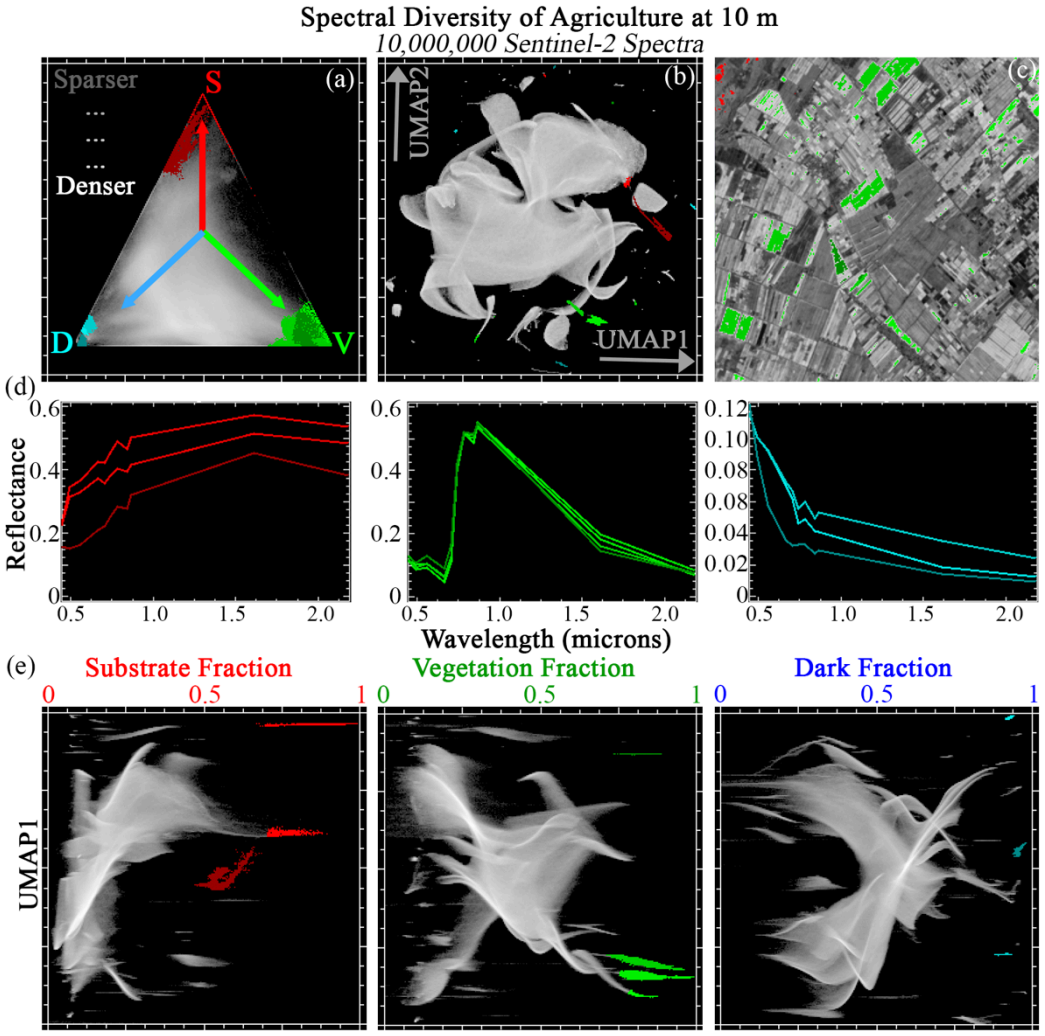

Figure 4. Joint characterization of agriculture. 10 x 1 megapixel Sentinel-2 tile subsets are selected from global agricultural hotpots and analyzed at full 10 m pixel resolution. These spectra fill out nearly the entire global SVD mixing space (top left) and are well represented by a single global 3-endmember linear mixture model (99% of spectra with <5% RMSE). Manifold learning (top center, using UMAP) captures both subtle mixing continua and discrete clusters, but does not offer physical interpretability. Joint characterization (bottom row) uses the physical meaning of the mixture fractions to contextualize the subtle statistical relationships captured by UMAP. Example regions of interest are identified from the joint space. Mean spectra for each region (center row) illustrate similarities and differences among statistically distinct clusters. Statistically distinct clusters identified through joint characterization frequently show geographic coherence (top right).

3.2. Sands

Figure 5 shows JC applied to a compilation of 10 tiles collected from geologically diverse sand dunes. As expected, the SVD ternary diagram (top left) shows a strong preferential distribution towards the global S endmember, with most mixing occurring along the S:D binary mixing line. Pixels with substantive V endmember contributions are effectively absent as few plants can grow in pure sand substrate. The sand spectra are well-fit by the global mixture model (99.9% spectra with <5% RMSE) – but fractions regularly exceed 100% due to frequently being brighter than the global soil endmember because of high solar incidence angle on sun-facing dune slopes. This suggests that differences between these spectra and the global S spectrum are largely driven by scaling of overall brightness, and not major changes in spectral curvature.

Examination of 2D UMAP embedding (top center) shows a discontinuous, sinuous manifold with numerous apexes and exterior pixel clusters. For JC of this land cover compilation, the S endmember fraction is the obvious choice for JC of this land cover compilation (bottom left).

Many high S distinct clusters are clearly identifiable from JC. 8 illustrative examples are shown in red and magenta. ROI mean spectra (bottom center) show variability consistent with potential physical drivers like grain size and mineralogy. Here, the S fraction effectively stratifies UMAP clusters by albedo, and UMAP effectively differentiates among subtle differences in spectral curvature among sands with similar albedos.

ROIs are geographically visualized on 2 example tiles (right column). ROI pixels consistently cluster on the basis of topographic position and geographic location in ways that strongly suggest physical meaning (e.g., fine vs coarse grain size at troughs vs dune crests). ROIs are again also back-projected onto both the SVD and UMAP spaces. From this back-projection, the complementarity captured by JC is again evident: UMAP clusters without EM fraction context lack physical context, and EM fractions without UMAP are visually indistinct.

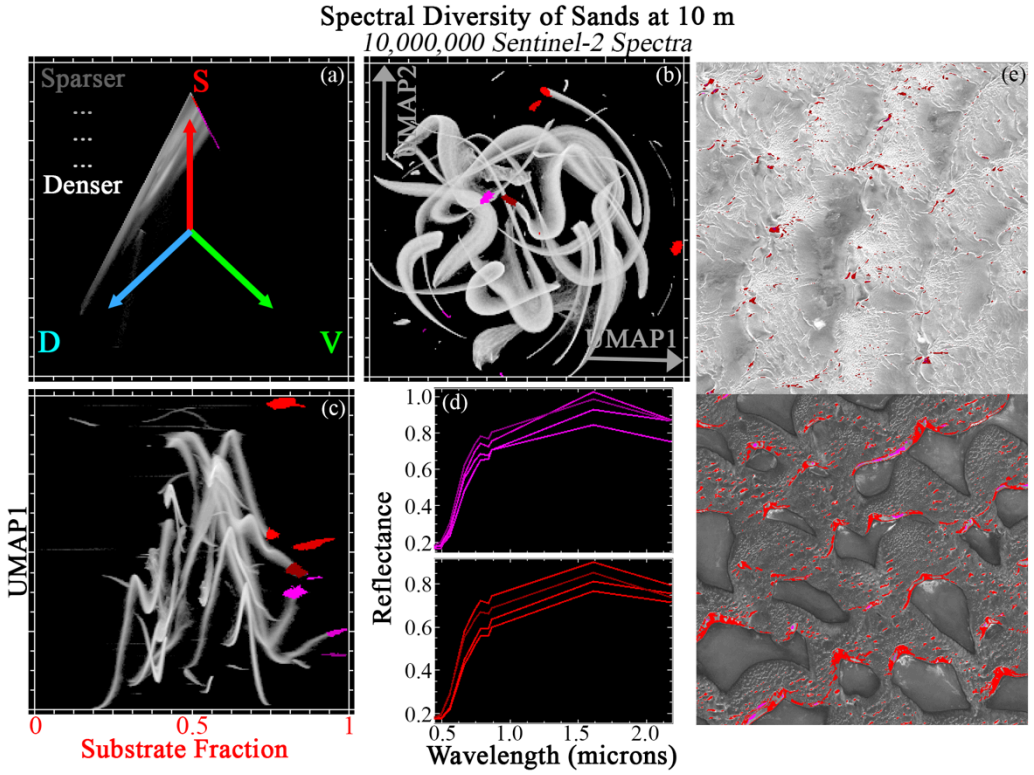

Figure 5. Joint characterization of sands. 10 x 1 megapixel Sentinel-2 tile subsets are selected from global sand hotspots and analyzed at full 10 m pixel resolution. These spectra preferentially occupy the S apex of the SVD mixing space, with mixing toward D (top left), leaving the V portion of the space very sparse. The global 3-endmember linear mixture model fits these spectra better than the agricultural spectra (here, only >99.9% of spectra with <5% RMSE) – but fractions regularly exceed 100%. UMAP (top center) captures both subtle mixing continua and discrete clusters, but does not offer physical interpretability. Joint characterization (bottom left) uses the physical meaning of the substrate mixture fraction to contextualize the subtle statistical relationships captured by UMAP. Example regions of interest are identified from the joint space and projected onto the ternary mixing and UMAP spaces. Mean spectra for each region (bottom center) illustrate similarities and differences among statistically distinct clusters. Clusters identified by joint characterization also frequently show geographic coherence (right column).

3.3. Lava/Ash

Figure 6 shows JC applied to a compilation of 5 tiles from globally diverse volcanic (lava and ash) landscapes. Within the global SVD mixing space, these landscapes are preferentially distributed between the D and S endmembers (top left). Some substantive mixing towards the V EM is also observed. Relative to the other land cover classes, these spectra are not particularly well fit by global mixture model (96.5% spectra with <5% RMSE). Presumably, this is because the global D endmember corresponds to clear, deep water – not ferromagnesian rock (e.g. basalt).

Examination of 2D UMAP embedding (top center) shows a set of interconnected submanifolds, each with numerous apexes and exterior pixel clusters. The S endmember fraction is again used to illustrate JC of this land cover compilation (bottom left).

Again, many distinct clusters with moderate to high S fraction are clearly identifiable from the JC. 8 of the clearest are shown in red and yellow. These ROIs are differentiated in terms of both overall albedo and spectral curvature across the full VSWIR range. The observed spectral variability is suggestive of differences in underlying (mafic : felsic) mineralogy, mineral vs glass composition (holocrystalline <-> holohyaline), texture (aphaneritic : phaneritic), and lava flow age/weathering.

ROIs are geographically visualized on 2 example tiles (right column). ROI pixels consistently cluster on the basis of topographic position and geographic location in ways that strongly suggest geophysical meaning (e.g. topographic position, across vs within individual flow extents). Back-projection of ROIs onto both SVD and UMAP spaces again highlights the complementarity of each characterization approach.

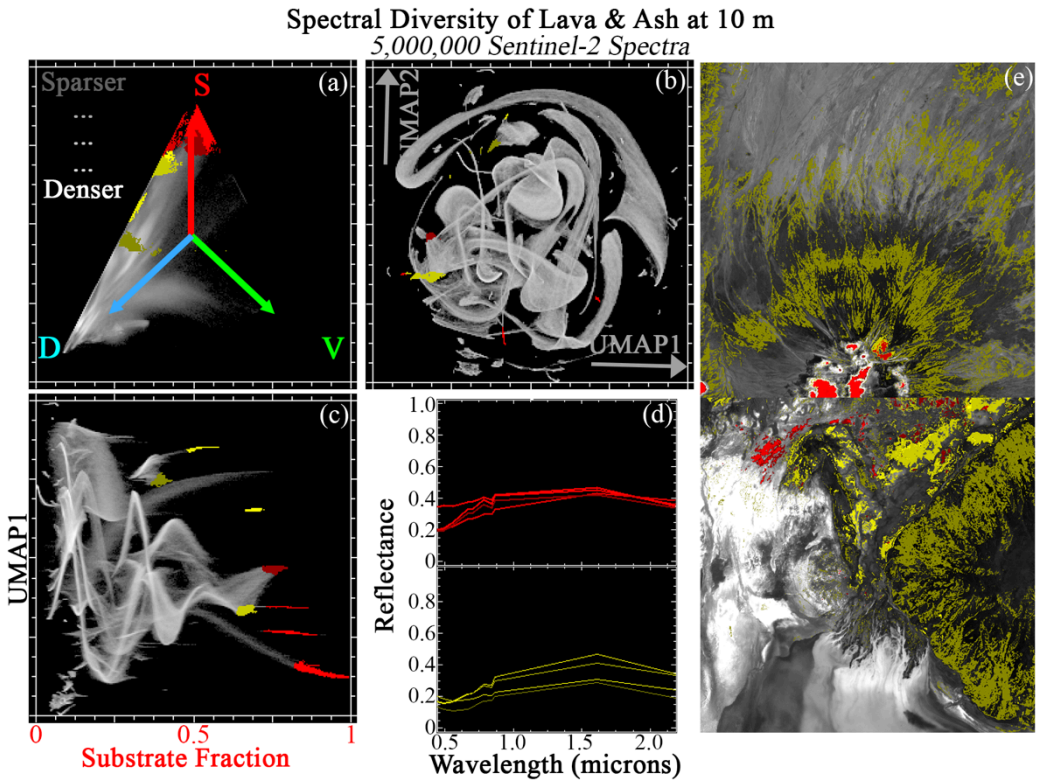

Figure 6. Joint characterization of Lava & Ash. 5 x 1 megapixel Sentinel-2 tile subsets are selected from global volcanic hotspots and analyzed at full 10 m pixel resolution. These spectra preferentially occupy the S to D apexes of the SVD mixing space (top left), leaving the V portion of the space relatively sparse. The global 3-endmember linear mixture model fits these spectra less well than the agricultural spectra (here, 96.5% of spectra with <5% RMSE). UMAP (top center) captures both subtle mixing continua and discrete clusters, but does not offer physical interpretability. Joint characterization (bottom left) uses the physical meaning of the Substrate mixture fraction to contextualize the subtle statistical relationships captured by UMAP. Example regions of interest are identified from the joint space and projected onto the ternary mixing and UMAP spaces. Mean spectra for each region (bottom center) illustrate similarities and differences among statistically distinct clusters. Clusters identified by joint characterization also frequently show geographic coherence (right column).

3.4. Urban

Figure 7 shows JC applied to a compilation of 5 tiles from globally diverse urban landscapes. Within the global SVD mixing space, these landscapes are preferentially distributed between the D and S endmembers (top left). More mixing towards the V EM is observed than with the volcanic or sand land cover classes. These spectra are better fit by the global mixture model than the volcanic compilation, but worse fit than the agriculture or sands (97.5% spectra with <5% RMSE).

Examination of 2D UMAP embedding (top center) shows a single, highly connected main manifold, with numerous apexes. This manifold is much more continuous than for the preceding land cover classes, with more dominant global structure and less prominent statistically local clustering. The S endmember fraction is again used to illustrate JC of this land cover compilation (bottom left).

Again, many distinct clusters are clearly identifiable from the JC. 8 of the clearest are shown in red and yellow. These ROIs are differentiated in terms of both overall albedo and spectral curvature across the full VSWIR range, particularly in the infrared spectral region. The observed spectral variability is suggestive of differences in synthetic materials (plastics, asphalt, roofing materials, paint), as well as exposed substrates.

ROIs are geographically visualized on 2 example tiles (right column). ROI pixels consistently cluster in ways suggestive of physical meaning (parking lots, roofs of large buildings, city blocks). Back-projection of ROIs onto both SVD and UMAP spaces again highlights the complementarity of each characterization approach.

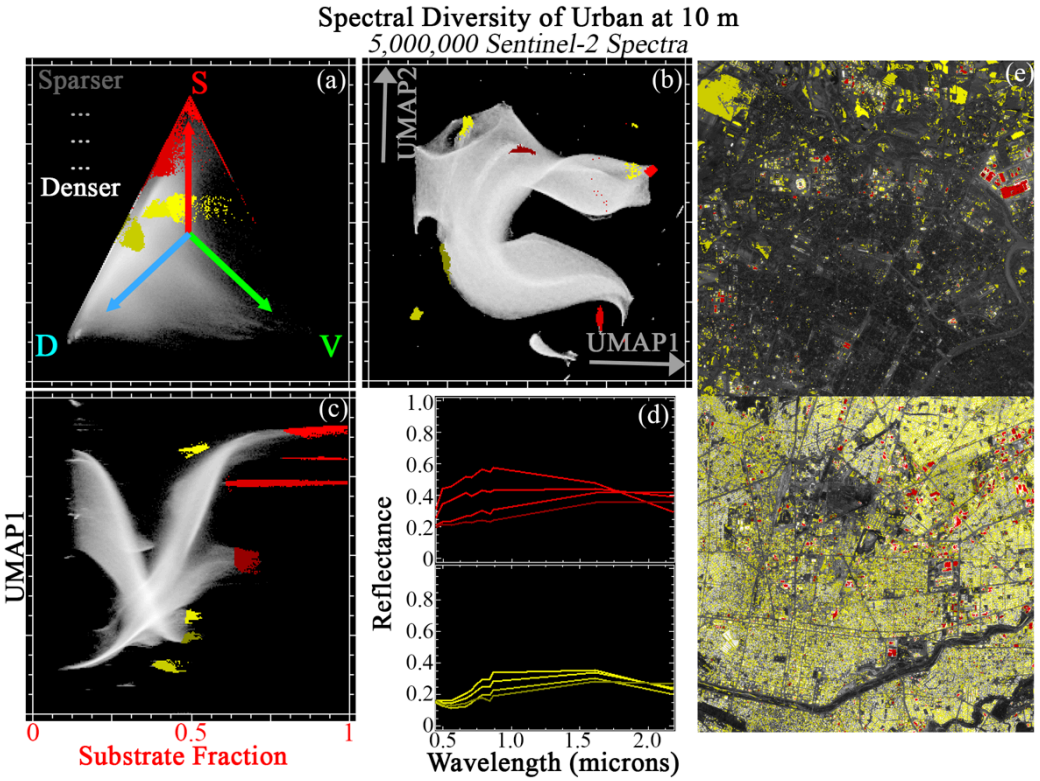

Figure 7. Joint characterization of urban landscapes. 5 x 1 megapixel Sentinel-2 tile subsets are selected from global urban hotspots and analyzed at full 10 m pixel resolution. These spectra fill out most of the SVD mixing space (top left). The global 3-endmember linear mixture model fits these spectra less well than the agricultural spectra (here, 97.5% of spectra with <5% RMSE). UMAP (top center) captures both subtle mixing continua and discrete clusters, but does not offer physical interpretability. Joint characterization (bottom left) uses the physical meaning of the Substrate mixture fraction to contextualize the subtle statistical relationships captured by UMAP. Example regions of interest are identified from the joint space and projected onto the ternary mixing and UMAP spaces. Mean spectra for each region (bottom center) illustrate similarities and differences among statistically distinct clusters. Clusters identified by joint characterization also frequently show geographic coherence (right column).

3.5. Forests

Figures 8 and 9 show JC applied to a compilation of 20 tiles (2 sets of 10) from globally diverse forests. Forest spectra are preferentially distributed towards the D:V mixing line (consistent with closed canopy spectra), with a significant amount of additional mixing towards S (consistent with incomplete canopy closure, stems and other woody material, and/or senescent leaves). The forest spectra are better fit by the global SVD mixture model than any preceding land cover class (99.9% spectra with <5% RMSE).

The 2D UMAP embedding (top center) shows a broad, well-connected manifold comprised of several major lobes. This manifold is visually less continuous than Urban, but more continuous than Sands or Lava/Ash. Multiple apexes to the main manifold and smaller disconnected pixel clusters are also present.

The V fraction is the natural endmember to use for Joint Characterization (bottom left). Useful manifold structure is observed at a wide range of V fractions. In each figure, 8 of the clearest are shown in cyan and green. These clusters are differentiated in terms of NIR amplitude (e.g., leaf structure), visible wavelength slope and curvature (e.g., pigments), and overall SWIR brightness (e.g., leaf water & dry matter).

In each figure, ROIs are geographically visualized on 2 example tiles (right column). As with other land cover classes, geographic clustering of ROIs (microtopography, distance from channel, ecological differences among tiles) implies plausible geophysical meaning. Back-projection of ROIs onto both SVD and UMAP spaces again highlights the complementarity of each characterization approach.

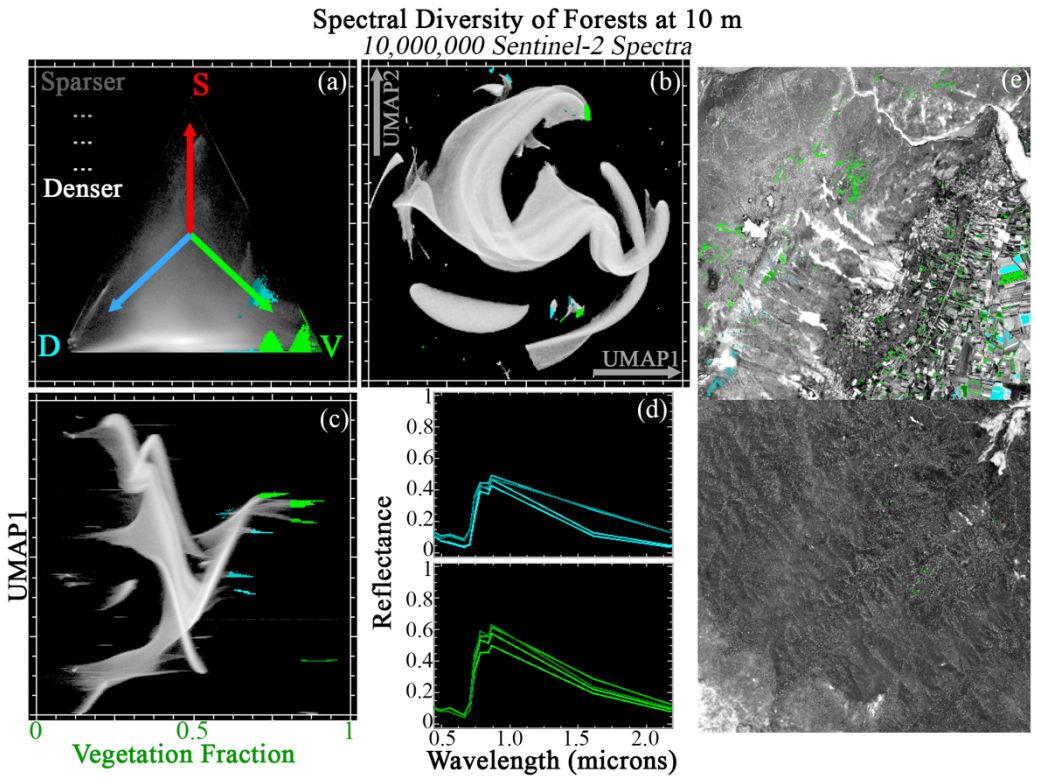

Figure 8. Joint characterization of forests (1). 10 x 1 megapixel Sentinel-2 tile subsets are selected from global forest diversity hotpots and analyzed at full 10 m pixel resolution. These spectra preferentially occupy the V to D apexes of the SVD mixing space (top left), leaving the S portion of the space relatively sparse. The global 3-endmember linear mixture model fits these spectra better than the agricultural spectra (here, > 99.9% of spectra with <5% RMSE). UMAP (top center) captures both subtle mixing continua and discrete clusters, but does not offer physical interpretability. Joint characterization (bottom left) uses the physical meaning of the Vegetation mixture fraction to contextualize the subtle statistical relationships captured by UMAP. Example regions of interest are identified from the joint space and projected onto the ternary mixing and UMAP spaces. Mean spectra for each region (bottom center) illustrate similarities and differences among statistically distinct clusters. Clusters identified by joint characterization also frequently show geographic coherence (right column).

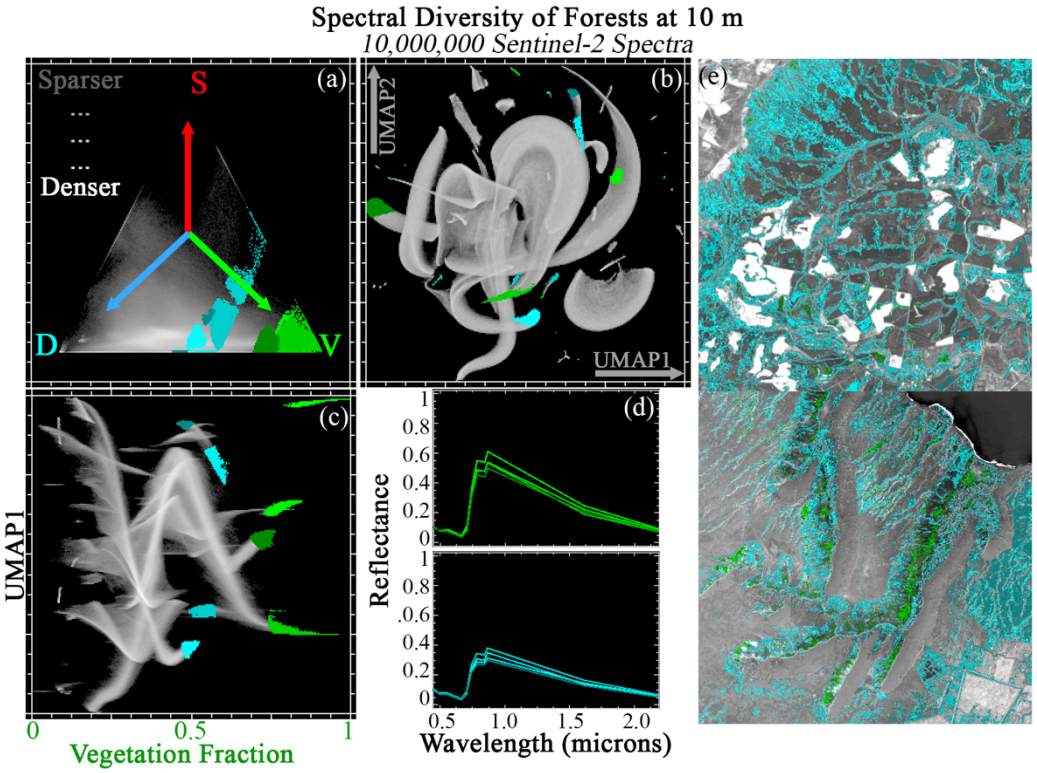

Figure 9. Joint characterization of forests (2). 10 x 1 megapixel Sentinel-2 tile subsets are selected from global forest diversity hotpots and analyzed at full 10 m pixel resolution. These spectra preferentially occupy the V to D apexes of the SVD mixing space (top left), leaving the S portion of the space relatively sparse. The global 3-endmember linear mixture model fits these spectra better than the agricultural spectra (here, > 99.9% of spectra with <5% RMSE). UMAP (top center) captures both subtle mixing continua and discrete clusters, but does not offer physical interpretability. Joint characterization (bottom left) uses the physical meaning of the Vegetation mixture fraction to contextualize the subtle statistical relationships captured by UMAP. Example regions of interest are identified from the joint space and projected onto the ternary mixing and UMAP spaces. Mean spectra for each region (bottom center) illustrate similarities and differences among statistically distinct clusters. Clusters identified by joint characterization also frequently show geographic coherence (right column).

3.6. Senescent Vegetation

Figure 10 shows JC applied to a compilation of 5 tiles from diverse biomes dominated by senescent vegetation. Within the global SVD mixing space, these landscapes are preferentially distributed towards high- to mid- Dark fraction values, with mixing towards both V and S endmembers well-represented, but less comprehensive than for the agriculture compilation (top left). Like the forest compilations, these spectra are also well fit by the global mixture model (99.9% spectra with <5% RMSE).

Examination of 2D UMAP embedding (top center) shows a single, highly connected main manifold. This continuity of this manifold is comparable to that of the urban land cover compilation. The V endmember fraction is again used to illustrate JC of this land cover compilation (bottom left).

Again, many clusters are clearly identifiable from the JC. 4 of the clearest V-dominated clusters are shown in green. 4 additional S-dominated clusters were selected from the S-based JC (not shown) and projected onto the V-based JC space. S-dominated ROIs are differentiated in terms of differences in NIR brightness and associated curvature. V-dominated ROIs are differentiated in terms of red edge bands and SWIR, along with NIR brightness. The observed spectral variability is suggestive of differences in overall vegetation composition and 3D structure (e.g., differences in volume scattering associated with grass vs shrub vs tree morphologies), as well as stage of senescence. V-dominated ROI differences are suggestive of leaf water (SWIR) and leaf structure (red edge, NIR), with one cluster showing significant differences in visible wavelength curvature in addition to a 50% reduction in NIR brightness. ROIs are geographically visualized on 2 example tiles (right column), and again cluster in ways suggestive of biophysical meaning (along river channels, stands of trees, discernable savanna transitions).

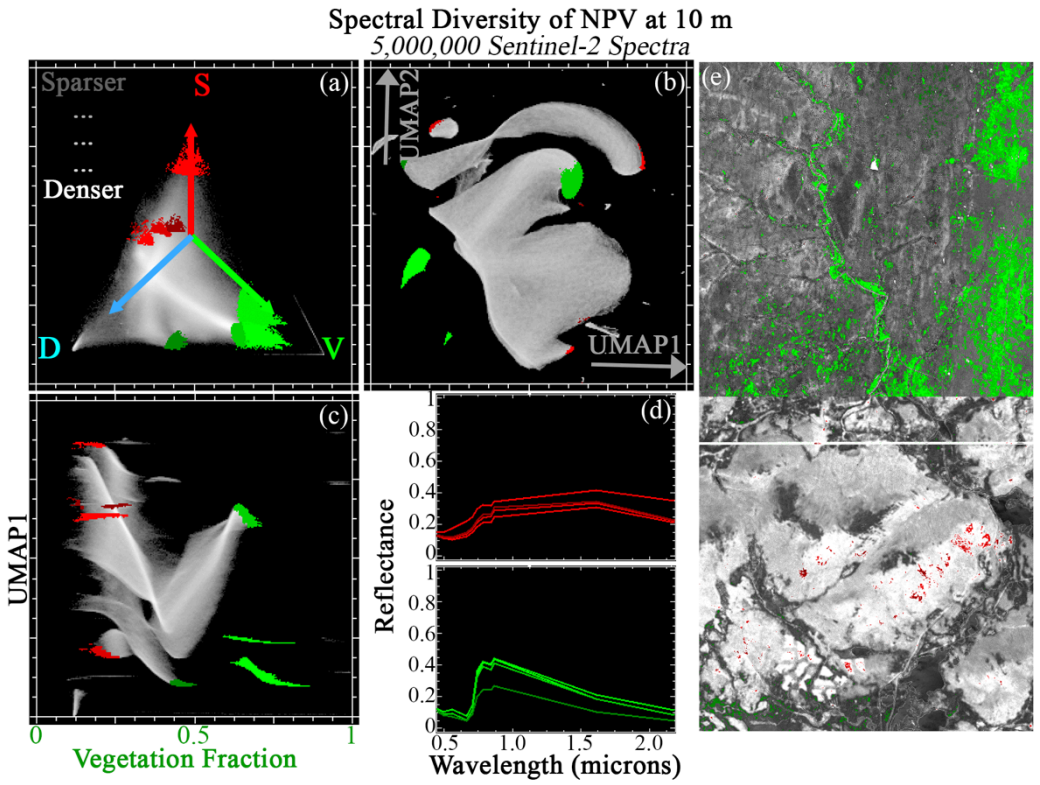

Figure 10. Joint characterization of senescent vegetation. 5 x 1 megapixel Sentinel-2 tile subsets are selected from global forest diversity hotpots and analyzed at full 10 m pixel resolution. These spectra preferentially occupy the V to D apexes of the SVD mixing space (top left), leaving the S portion of the space relatively sparse. The global 3-endmember linear mixture model fits these spectra better than the agricultural spectra (here, 99.9% of spectra with <5% RMSE). UMAP (top center) captures both subtle mixing continua and discrete clusters, but does not offer physical interpretability. Joint characterization (bottom left) uses the physical meaning of the Vegetation mixture fraction to contextualize the subtle statistical relationships captured by UMAP. Example regions of interest are identified from the joint space and projected onto the ternary mixing and UMAP spaces. Mean spectra for each region (bottom center) illustrate similarities and differences among statistically distinct clusters. Clusters identified by joint characterization also frequently show geographic coherence (right column).

3.7. Tundra

Figure 11 shows JC applied to a compilation of 5 tiles from diverse tundra landscapes. Within the global SVD mixing space, these landscapes are preferentially the D <-> V mixing line (consistent with dense vegetation and vegetation/water mixtures), with minor additional mixing towards S (consistent with dark, water-saturated soils) (top left). Like the forest and senescent vegetation compilations, these spectra are well fit by the global mixture model (99.8% spectra with <5% RMSE).

Examination of 2D UMAP embedding (top center) shows a single main manifold with several lobes. This manifold is less continuous than the urban or senescent vegetation compilations, but more continuous than the sand or volcanic compilations. Here, the D endmember fraction is used to illustrate JC of this land cover compilation (bottom left).

Again, many clusters are clearly identifiable from the JC. 4 of the clearest D-dominated clusters are shown in cyan. 4 additional low-D (and high V) clusters were also selected (shown in green). D-dominated ROIs are differentiated in terms of overall brightness in the NIR and SWIR (turbidity/flotsam?) and curvature in the visible (chlorophyll, CDOM?). V-dominated ROIs are differentiated in terms of NIR amplitude (plant community structure?), visible wavelength slope and curvature (pigments?), and overall SWIR brightness (canopy & understory water? Spatial mixing with underlying waterlogged substrate?). ROIs are geographically visualized on 2 example tiles (right column), and again cluster in ways highly suggestive of biophysical meaning (V: distance from river channel, microtopography, differences among tiles; D: sets of thermokarst lakes clustering together, possibly on the basis of lake age, largely distinct from river channels).

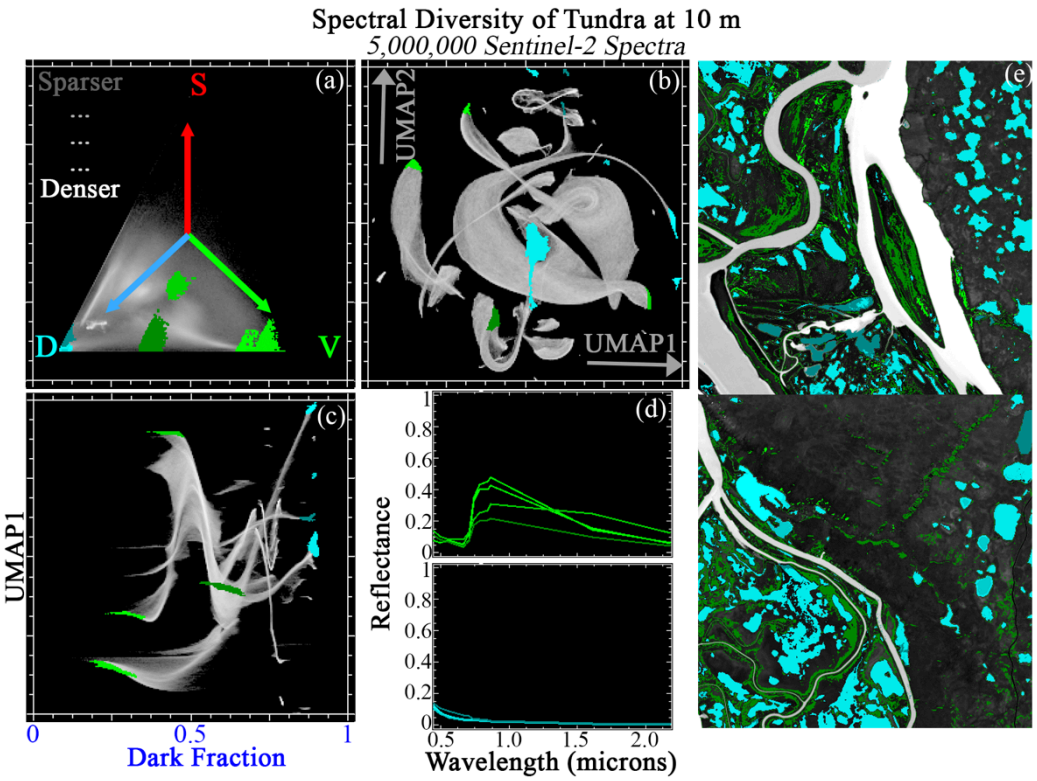

Figure 11. Joint characterization of tundra. 5 x 1 megapixel Sentinel-2 tile subsets are selected from global tundra diversity hotpots and analyzed at full 10 m pixel resolution. These spectra preferentially occupy the V to D apexes of the SVD mixing space (top left), leaving the S portion of the space relatively sparse. The global 3-endmember linear mixture model fits these spectra better than the agricultural spectra (here, 99.8% of spectra with <5% RMSE). UMAP (top center) captures both subtle mixing continua and discrete clusters, but does not offer physical interpretability. Joint characterization (bottom left) uses the physical meaning of the Dark mixture fraction to contextualize the subtle statistical relationships captured by UMAP. Example regions of interest are identified from the joint space and projected onto the ternary mixing and UMAP spaces. Mean spectra for each region (bottom center) illustrate similarities and differences among statistically distinct clusters. Clusters identified by joint characterization also frequently show geographic coherence (right column).

3.8. Mangroves and Wetlands

Figure 12 shows JC applied to a compilation of 10 tiles from diverse mangrove and wetland landscapes. Mixture fractions from these landscapes are distributed similarly to tundra, preferentially occurring near the D:V mixing line, with minor additional mixing towards S (consistent with more open canopies resulting in subpixel mixing with water or dark, water-saturated soils) (top left). Like the forest, senescent vegetation, and tundra compilations, these spectra are well fit by the global mixture model (99.9% spectra with <5% RMSE).

Examination of 2D UMAP embedding (top center) shows a single main manifold with several lobes. This manifold also comparable to the tundra compilation: less continuous than the urban or senescent vegetation compilations, but more continuous than the sand or volcanic compilations. Here, the V endmember fraction is used to illustrate the JC approach (bottom left).

Again, many submanifolds are clearly identifiable as apexes and clusters from the JC. 8 of the clearest V-dominated clusters are shown in cyan and green. 4 additional low-D (and high V) clusters were also selected (shown in green). D-dominated ROIs are differentiated in terms of overall brightness in the NIR and SWIR (turbidity/flotsam?) and curvature in the visible (chlorophyll, CDOM?). V-dominated ROIs are differentiated in terms of NIR amplitude (possibly associated with leaf and canopy structure), visible wavelength slope and curvature (potentially associatd with pigments), and overall SWIR brightness (potentially associated with canopy and/or understory water, and spatial mixing with an underlying waterlogged substrate). ROIs are geographically visualized on 2 example tiles (right column), and again cluster in ways highly suggestive of biogeophysical meaning (distance from river channel, microtopography, differences among tiles).

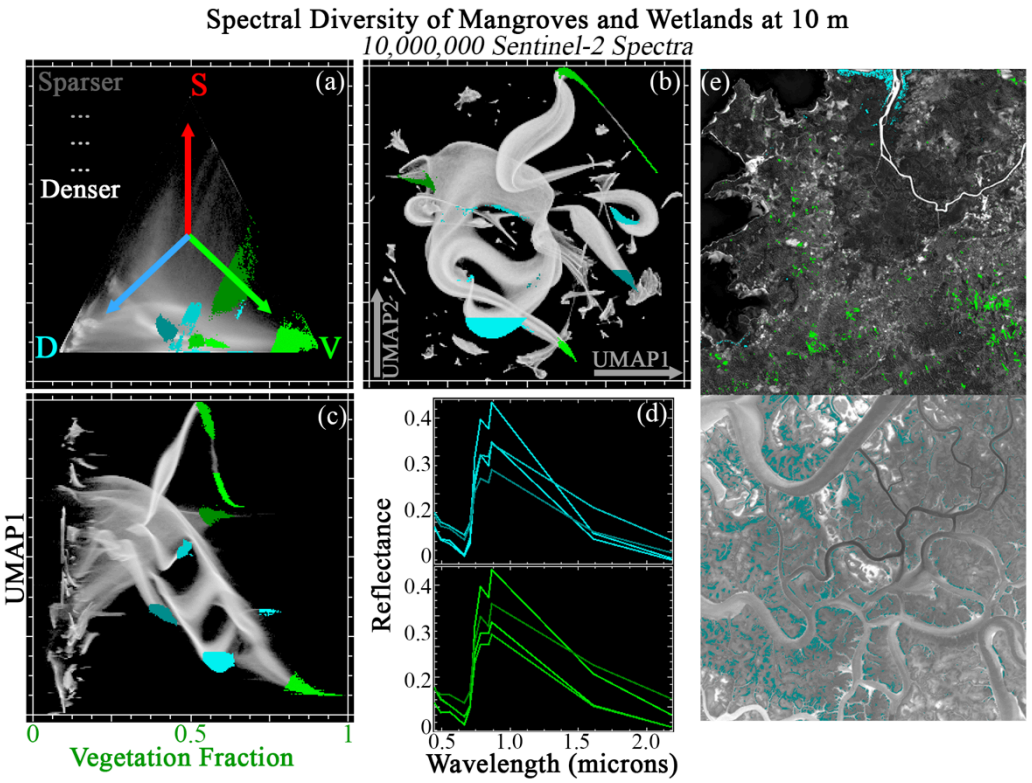

Figure 12. Joint characterization of mangroves and wetlands. 10 x 1 megapixel Sentinel-2 tile subsets are selected from global forest diversity hotpots and analyzed at full 10 m pixel resolution. These spectra preferentially occupy the V to D apexes of the SVD mixing space (top left), leaving the S portion of the space relatively sparse. The global 3-endmember linear mixture model fits these spectra better than the agricultural spectra (here, > 99.9% of spectra with <5% RMSE). UMAP (top center) captures both subtle mixing continua and discrete clusters, but does not offer physical interpretability. Joint characterization (bottom left) uses the physical meaning of the Vegetation mixture fraction to contextualize the subtle statistical relationships captured by UMAP. Example regions of interest are identified from the joint space and projected onto the ternary mixing and UMAP spaces. Mean spectra for each region (bottom center) illustrate similarities and differences among statistically distinct clusters. Clusters identified by joint characterization also frequently show geographic coherence (right column).

3.9. Rocks and Alluvium

Figures 13 and 14 show JC applied to a compilation of 20 tiles (2 sets of 10) from geologically diverse landscapes exemplifying rock and alluvium, respectively. Both rock and alluvium spectra are preferentially distributed towards the D:S mixing line, with minor mixing towards V within the global SVD mixing space (upper left). Like the lava/ash spectra, these spectra are less well fit by the global mixture model (96% spectra with <5% RMSE), presumably because the single Substrate EM does not capture the full geologic diversity of the basement rocks and alluvium.

The 2D UMAP embedding (top center) shows a broad, well-connected manifold comprised of several major lobes. These manifolds are visually less continuous than Urban, but more continuous than Sands or Lava/Ash. Multiple apexes to the main manifold and smaller disconnected pixel clusters are also present.

Here, the S fraction is the natural endmember to use for JC (bottom left). Useful manifold structure is observed at a wide range of S:D mixture fraction continuum. In each figure, 8 of the clearest apexes and clusters are shown. These ROIs are differentiated in terms of both overall albedo and spectral curvature across the full VSWIR range. Mean cluster spectra are suggestive of differences in underlying (mafic : felsic) mineralogy, rock type (igneous, sed, met), exposure age/weathering, hydrothermal alteration, presence/absence of evaporite minerals.

In each figure, ROIs are geographically visualized on 2 example tiles (right column). As with other land cover classes, geographic clustering of ROIs (topographic position, relation to extraction operations) identified from JC implies plausible geophysical meaning. Back-projection of ROIs onto both SVD and UMAP spaces again highlights the complementarity of each characterization approach.

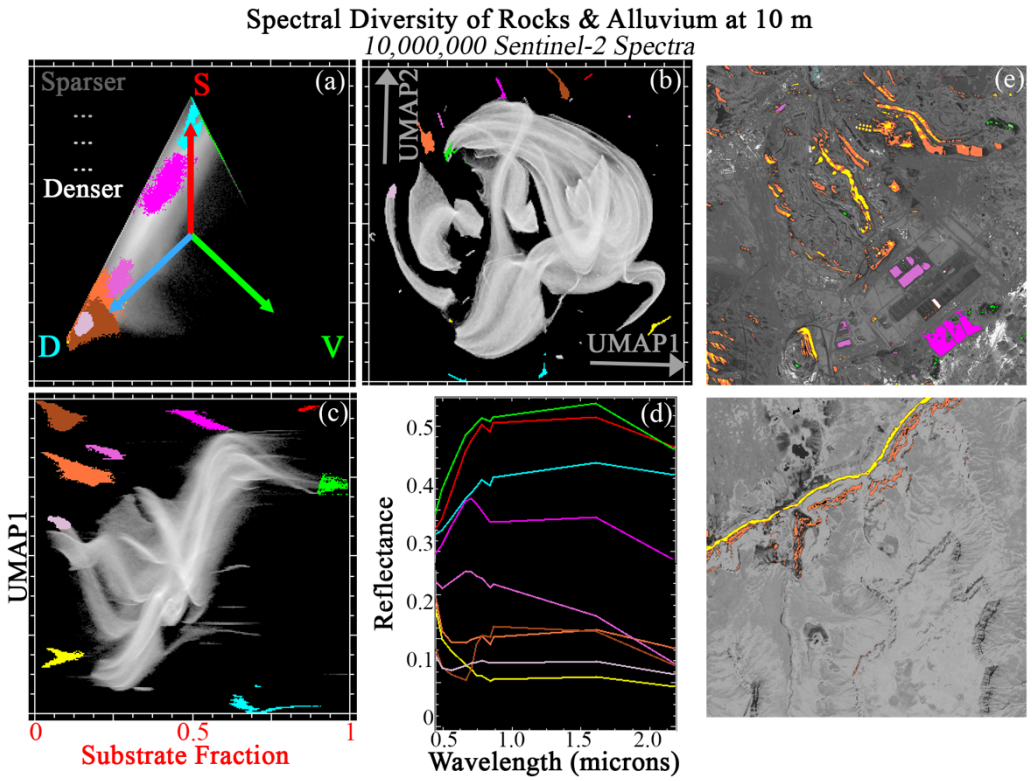

Figure 13. Joint characterization of rocks and alluvium (1). 10 x 1 megapixel Sentinel-2 tile subsets are selected from global geology hotspots and analyzed at full 10 m pixel resolution. These spectra preferentially occupy the S to D apexes of the SVD mixing space (top left), leaving the V portion of the space relatively sparse. The global 3-endmember linear mixture model fits these spectra less well than the agricultural spectra (here, only 96% of spectra with <5% RMSE). UMAP (top center) captures both subtle mixing continua and discrete clusters, but does not offer physical interpretability. Joint characterization (bottom left) uses the physical meaning of the Substrate mixture fraction to contextualize the subtle statistical relationships captured by UMAP. Example regions of interest are identified from the joint space and projected onto the ternary mixing and UMAP spaces. Mean spectra for each region (bottom center) illustrate similarities and differences among statistically distinct clusters. Clusters identified by joint characterization also frequently show geographic coherence (right column).

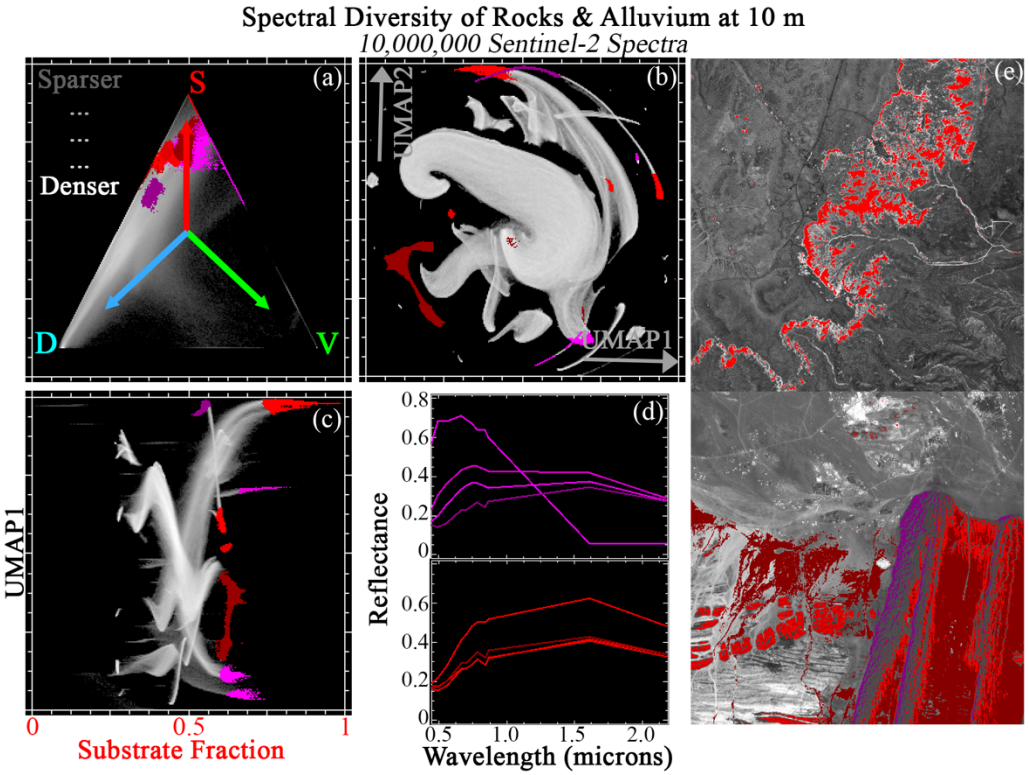

Figure 14. Joint characterization of rocks and alluvium (2). 10 x 1 megapixel Sentinel-2 tile subsets are selected from global geology hotspots and analyzed at full 10 m pixel resolution. These spectra preferentially occupy the S to D apexes of the SVD mixing space (top left), leaving the V portion of the space relatively sparse. The global 3-endmember linear mixture model fits these spectra less well than the agricultural spectra (here, 98.5% of spectra with <5% RMSE). UMAP (top center) captures both subtle mixing continua and discrete clusters, but does not offer physical interpretability. Joint characterization (bottom left) uses the physical meaning of the Substrate mixture fraction to contextualize the subtle statistical relationships captured by UMAP. Example regions of interest are identified from the joint space and projected onto the ternary mixing and UMAP spaces. Mean spectra for each region (bottom center) illustrate similarities and differences among statistically distinct clusters. Clusters identified by joint characterization also frequently show geographic coherence (right column).

4. Discussion

With these results in mind, we structure our discussion in three parts. First, we revisit each of the fundamental science questions that motivated this analysis. Next, we present an explanation for the underlying reasoning behind the effectiveness of the method. We then close with a brief discussion of limitations, avenues for future work, and concluding remarks.

4.1. Revisiting the Motivating Questions

4.1.1. Question 1: Variance-Based Characterization & Modeling

The first set of questions addressed by this study concerned the overall SVD fraction (and misfit) distributions of globally significant land cover classes. The SVD fraction question is addressed by the ternary diagrams shown in the upper left of each of Figures 4 through 14. We summarize this information in Figure 15, showing the SVD distribution for each land cover class (outer plots), as well as the merged global distribution of the entire mosaic (center left). Clearly, the land cover classes used in this study occupy overlapping subsets of the global SVD space. This is in part because

spectral mimicking may render distinct reflectances indistinguishable with a broadband sensor, and in part because not all land cover categories are fully mutually exclusive of each other. For example, some rock and alluvium subsets certainly contain some amount of green and senescent vegetation, as well as some sand, and some mangroves extend into the forest continuum.

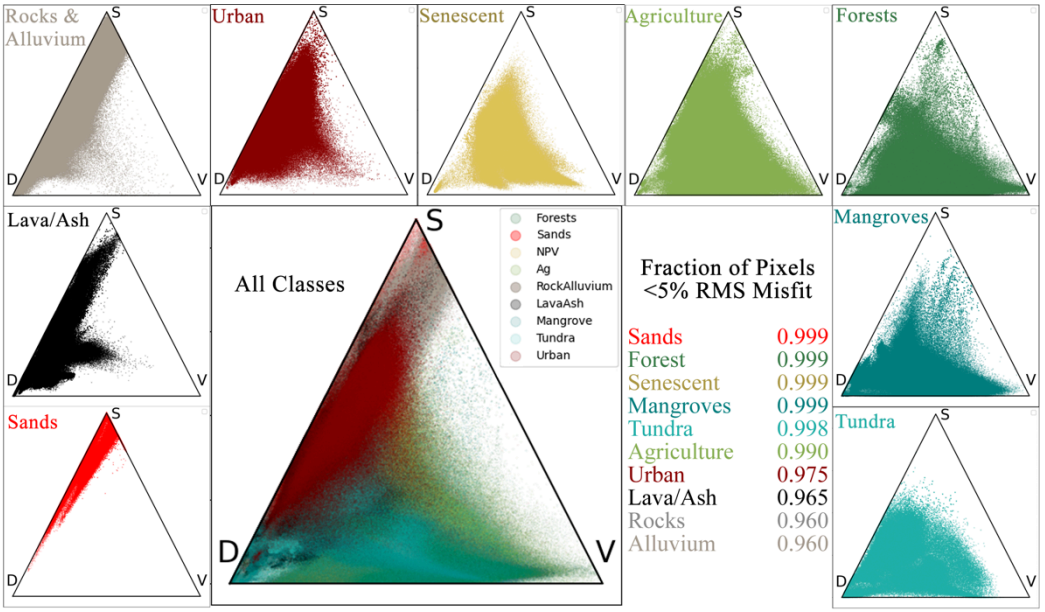

Figure 15. SVD fractions summarized by land cover type. Sands are dominated by S. Other geologic scenes show more mixing towards D. Urban, senescent, and agriculture show increasing mixing towards V, respectively. Forests, mangroves, and tundra then show decreasing S and increased skew towards binary V:D mixing, respectively.

Despite this fundamental nonuniqueness observed in SVD fraction space, differences among land cover class distributions are also evident. Specifically, agricultural landscapes (light green) are the most spectrally variable of all the classes, spanning nearly the entire space SVD space. Forests, mangroves, tundra (dark green, dark cyan, and cyan, respectively) are reasonably well mixed, but preferentially occur towards the D:V binary. Urban landscapes (dark red) are also reasonably mixed, but instead skew towards the D:S binary. Rocks, alluvium, and lava/ash (dark gray, dark brown, and black) are further skewed towards the D:S binary, and the sands used in this compilation (red) demonstrate this preferential distribution even more strongly.

Mixture model misfit also varies by land cover category (Figure 15, center right). Classes dominated by closed canopies, exposed soil, and water tend to yield relatively low misfits (5% error or less for >99% of pixel spectra). Classes with the highest misfit are likely to host greater substrate diversity than can be captured by a simple 3 EM model. This can take the form of either geologic (rock, soil, alluvium, lava/ash) or synthetic (urban) materials. Notably, even for these poorer-fit landscapes, the vast majority (>95%) of pixels still show root mean square misfits < 5%.

4.1.2. Question 2: Topology-Based Characterization & Modeling

The second set of questions concerns category dependence of the underlying topology of the spectral data manifold. These questions are addressed by the UMAP manifolds in the top center of each of Figures 4 through 14, summarized for convenience along the periphery of Figure 16.

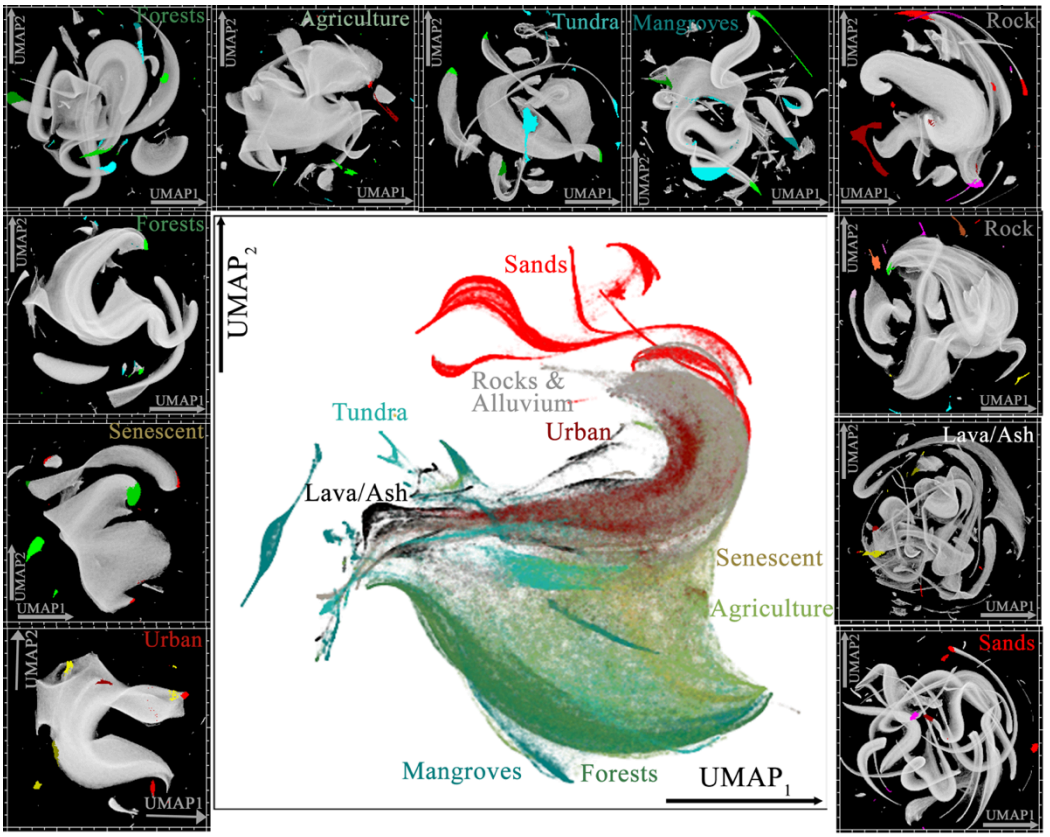

Figure 16. UMAP summary. Urban and senescent show highly continuous manifolds. Forests, agriculture, tundra, and mangrove show increasing clustering/decreasing continuity, respectively. Of the geologic scenes, rocks and alluvium show more continuous manifolds, with lava/ash and sands showing highly sinuous, clustered manifolds with a large number of distinct apexes.

Spectral manifold topology can clearly vary considerably across land cover types. In some cases, UMAP learns a single, well-connected manifold with a relatively small number of apexes and exterior clusters (e.g., Urban, Senescent Vegetation). In other cases, substantially more sinuous manifolds are found with more complex apexes and disconnected exterior clusters (e.g., Sands, Lava/Ash). Other land cover classes yield intermediate results.

4.1.3. Question 3: Leveraging Variance & Topology with Joint Characterization

The third set of questions we address concerns the practical utility of the joint (SVD + UMAP) characterization approach. These questions are addressed by the joint characterization plots and associated spectra shown in the lower portion of Figures 4-14, and geographic patterns shown in the right columns. For brevity, these are not summarized in an additional figure here.

Clearly, JC consistently succeeds in using SVD fractions to differentiate UMAP clusters on the basis of physical interpretability. JC-identified ROIs frequently demonstrate geographical coherence and spectrally interpretability from physically-based absorption features and scattering processes. In addition, JC produces potentially useful results even when overall spectral variance, spectral curvature, geographic size/contiguity of landscape features, and generative physical processes vary considerably across land cover types. Further, JC seems to be equally effective at capturing potentially useful clustering relations when landscapes are dominated by either S, V, or D endmember fractions.

4.2. Why JC Works: A Convergence of Visions

The preceding analysis clearly demonstrates that JC is effective at identifying subtle, spatially coherent, spectrally distinct patterns in multispectral imagery. But why does this approach work? Here we present the philosophy underlying the approach context of two complementary visions for analysis of high dimensional imagery.

4.2.1. The Geophysical Vision: Projecting each Pixel Spectrum Independently onto the Global Mixing Space

One vision for the analysis of spectral imagery conceptualizes the problem geophysically. This approach is rooted in a long line of physically-based characterization and modeling which has been formalized by the field of geophysical inverse theory [48–50]. In the context of the present study, this framework considers the image analysis problem to be physical, linear, and deterministic. A specific, interpretable quantity is estimated (e.g., area contribution of constituent EMs). Some prior knowledge of the system is required – which fortunately has been obtained by previous studies characterizing the global spectral mixing space ([43,44,36] and subsequent papers). This knowledge is used to design a system of equations which can be formulated into a matrix which describes a specific set of linear mixing processes governing the interaction of incident solar radiation with the Earth surface. Only 1 tunable parameter (weight of unit sum constraint), rationale for parameter choice (1.0) has quasi-physical basis. A key assumption of this approach is that *global variance* is representative of information content. This assumption is intrinsically linked to the choice of error metric (or cost function), which is commonly selected as the l_2 norm. Inverting the linear mixture model to obtain estimates of EM fractions provides a continuous result that is easily validated by comparison with higher spatial resolution imagery (vicarious validation) or in situ field measurements.

4.2.2. The Statistical Vision: Learning High-Dimensional Structure Within and Among Clusters of Similar Pixel Spectra

Another vision for the analysis of spectral imagery conceptualizes the problem purely statistically. This approach is rooted in the more recently developed field of manifold learning, e.g. as reviewed by [16] and implemented for hyperspectral image analysis by [51,52]. Here, no physical model is assumed. Instead, the pixel spectra and aggregate mixing space are treated purely statistically. Linearity is not assumed, and models generally have a stochastic element. The problem of characterization is formulated in terms of estimation of an abstract quantity (i.e., optimal embedding of a natively high-D manifold into a low-D space). Prior physical knowledge is not required, nor is it used. But several tunable parameters exist, which have the potential to significantly alter the end result. Often a parameter is used to quantify connective complexity by setting a number of statistical neighbors to be examined. In this context, hyperparameter choice is less defensibly physical (although arguments can be made for a link to spatial autocorrelation). The key assumption of this approach is that *local topology* is representative of information content. For this analysis, hyperparameter sensitivity is treated in the supplementary materials.

4.2.2. Fusing These Two Visions: Joint Characterization

JC was designed under the guiding principle that both the geophysical and statistical visions have intrinsic merit for the generalized problems of characterization and modeling of spectral imagery. Specifically, a framework was desired which could use the strengths the geophysical vision to mitigate the limitations of the statistical vision, and vice versa.

The fundamental idea of JC is to use two (or more) different formalizations of information to characterize, and ultimately model, high dimensional information. Conceptually, this can be understood using an analogy to parallax – systems capable of observing the world from two lines of sight can use both the redundancy and variability in the signals captured by each to estimate information not generally evident from either vantage point alone.

Here, we use SVD mixture fractions as our geophysical metric, and one UMAP dimension as our statistical metric. The approach could easily be extended to 3D (e.g. 1 SVD + 2 UMAP dimensions) or higher dimensions by using 3D UMAP projections and three (or more) fraction dimensions. When implementing JC in this context: mixture fractions give physically interpretable information capable of discriminating among UMAP-identified clusters; and UMAP embeddings give statistical information capable of separating subtle spectral features which are not evident from mixture fractions alone.

4.3. Limitations and Future Work

4.3.1. Limitations

Like any analysis approach, JC is not without limitations. One important consideration is the nonuniqueness of the manifold learning output. A wide range of possible algorithms exist, and more are certain to be developed in the coming decades. While we use UMAP here, we note that t-SNE [53] and Laplacian Eignemaps [54] can also prove useful, for instance as shown in [28–30]. Other algorithms also possess important strengths and weaknesses. Similarly, these algorithms tend to have stochastic elements and require prescription of several tunable parameters; implementation always has the potential to be sensitive to hyperparameter choice and users are advised to examine the severity of this limitation on a case-by-case basis (e.g., [55]). Anecdotally, we do note that our experience suggests UMAP outputs are less likely to be plagued by severe issues in this regard than some other algorithms[56–58].

In addition, the manifold learning step is fundamentally dependent on the spatial resolution of the imagery in a way that SVD fractions are not. V fractions in particular, and SVD fractions more generally, have been shown to scale linearly from meter to kilometer ground sampling distance [37,39,59]. While global EMs are identified from spectrally diverse, PC-derived, aggregate spectral mixing spaces, each pixel's SVD fractions are estimated independently from all other pixels, and are not sensitive to the overall number of samples. This is inherently not the case for manifold learning algorithms. Anecdotal results from spectral libraries and collections of leaf-level reflectance spectra are substantially less fruitful than results for full images. It is thus possible that the manifold learning aspect of JC may require the redundancy that is provided by image spatial autocorrelation to reach its potential.

We further note that this workflow is not, at present, fully automatable. We do not find present methods of automatic cluster detection to yield satisfactory results in the context of JC. This approach can thus be considered semi-supervised, with final interactive input from the scientist to select the clusters and apexes for regions of interest.

Finally, the globally standardized 3-endmember SVD model intentionally excludes some optically complex landscapes – notably, evaporites, cryosphere, and shallow marine envrironments. Reflectance images containing these features will not be accurately modeled by the global SVD endmembers, and so JC will be of minimal use. However, the wavelength-dependent mixture residual of the generalized global model may contain a significant amount of useful information, as suggested by [41], and applying JC to mixture residual images of this landscape may be significantly more useful in these cases.

4.3.2. Future Work

A wide range of promising avenues exist for integrating JC into image analysis workflows. One category of future work involves integration with advances in data quality and quantity. For instance, JC has the potential to improve characterization and modeling of hyperspectral imagery (e.g., through recent & planned missions like EMIT [60], DESIS [61], PRISMA [62], CHIME [63], HISUI [64], and SBG [65]), as well as spatially and temporally dense image time series (e.g., Sentinel-2 and Planet imagery). Hyperspectral applications are particularly promising given its greater reported intrinsic dimensionality [66–70]. Application to field- and tower-based imagery is also promising.

As noted above, another avenue for investigation is the incorporation of other algorithms and other information metrics. Several other nonlinear dimensionality reduction algorithms exist for this purpose beyond UMAP and t-SNE, like Laplacian Eigenmaps [54], ISOMAP [71], and both metric and nonmetric multidimensional scaling (MDS and NMDS, [72,73]). Similarly, other geophysical observed (emissivity, land surface temperature, night light luminance) and/or modeled (evapotranspiration, population density) parameters could be used as well.[29]

5. Conclusions

We demonstrate Joint Characterization (JC), a novel approach for spectral image analysis, using a globally diverse mosaic of 90,000,000 Sentinel-2 image spectra. JC exploits synergy between geophysical (spectral mixture analysis) and topological (manifold learning) approaches to characterization and modeling. Dependence of both approaches on land cover is examined through detailed investigation of 10 categories. For each class, mixture fraction distribution and spectral manifold topology are characterized, and JC is shown to effectively capture clusters and apexes which are clearly geographic coherent and spectrally distinct. The underlying philosophy of the method, its major limitations, and avenues for future work are discussed. Taken together, these results highlight the potential of JC as an effective, efficient approach for characterization and modeling of high dimensional image information.

Supplementary Materials: The following supporting information can be downloaded at: www.mdpi.com/xxx/s1, Figure S1: title; Table S1: title; Video S1: title.

Author Contributions: For research articles with several authors, a short paragraph specifying their individual contributions must be provided. The following statements should be used "Conceptualization, X.X. and Y.Y.; methodology, X.X.; software, X.X.; validation, X.X., Y.Y. and Z.Z.; formal analysis, X.X.; investigation, X.X.; resources, X.X.; data curation, X.X.; writing—original draft preparation, X.X.; writing—review and editing, X.X.; visualization, X.X.; supervision, X.X.; project administration, X.X.; funding acquisition, Y.Y. All authors have read and agreed to the published version of the manuscript." Please turn to the CRediT taxonomy for the term explanation. Authorship must be limited to those who have contributed substantially to the work reported.

Funding: DS gratefully acknowledges funding from the USDA NIFA Sustainable Agroecosystems program (Grant # 2022-67019-36397), the NASA Land-Cover/Land Use Change program (Grant # NNH21ZDA001N-LCLUC), the NASA Remote Sensing of Water Quality program (Grant # 80NSSC22K0907), and the NSF Signals in the Soil program (Award # 2226649). CS acknowledges the support of the endowment of the Lamont Doherty Earth Observatory.

Data Availability Statement: In this section, please provide details regarding where data supporting reported results can be found, including links to publicly archived datasets analyzed or generated during the study. Please refer to suggested Data Availability Statements in section "MDPI Research Data Policies" at https://www.mdpi.com/ethics. If the study did not report any data, you might add "Not applicable" here.

Acknowledgments: The authors thank Brother Tom for philosophical inspiration.

Conflicts of Interest: The authors declare no conflict of interest.

Appendix A

Here we include a supplementary figure showing hyperparameter dependence, and a supplementary table showing the Sentinel-2 Scene IDs used in this analysis.

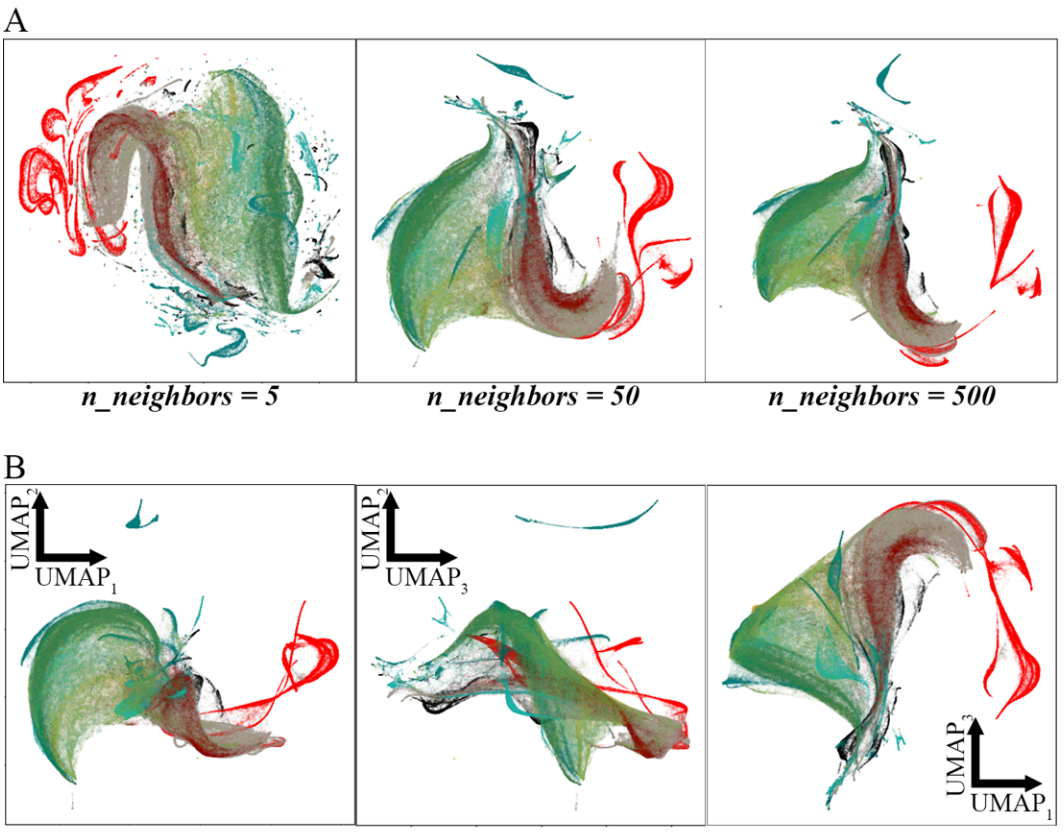

Figure S1. Hyperparameter dependence. dependence. Panel A: Impact of the n_neighbors parameter, illustrated for the full labeled mosaic across 2 orders of magnitude. Fewer neighbors generally results in a more clustered and less continuous manifold. Panel B: Effect of using a 3D embedding space, compared to the 2D spaces shown throughout this analysis.

Table S1. Scene list.

References

1. Landgrebe, D.; Hoffer, R.; Goodrick, F. An Early Analysis of ERTS-1 Data. **1972**.
2. Straub, C.L.; Koontz, S.R.; Loomis, J.B. Economic Valuation of Landsat Imagery. *Open-File Report-US Geological Survey* **2019**.
3. Zhu, Z.; Wulder, M.A.; Roy, D.P.; Woodcock, C.E.; Hansen, M.C.; Radeloff, V.C.; Healey, S.P.; Schaaf, C.; Hostert, P.; Strobl, P. Benefits of the Free and Open Landsat Data Policy. *Remote Sensing of Environment* **2019**, *224*, 382–385.
4. Landgrebe, D. Machine Processing for Remotely Acquired Data. *LARS Technical Reports* **1973**, 29.
5. Price, J.C. Spectral Band Selection for Visible-near Infrared Remote Sensing: Spectral-Spatial Resolution Tradeoffs. *IEEE Transactions on Geoscience and Remote Sensing* **1997**, *35*, 1277–1285, doi:10.1109/36.628794.
6. Wulder, M.A.; Roy, D.P.; Radeloff, V.C.; Loveland, T.R.; Anderson, M.C.; Johnson, D.M.; Healey, S.; Zhu, Z.; Scambos, T.A.; Pahlevan, N. Fifty Years of Landsat Science and Impacts. *Remote Sensing of Environment* **2022**, *280*, 113195.
7. Drusch, M.; Del Bello, U.; Carlier, S.; Colin, O.; Fernandez, V.; Gascon, F.; Hoersch, B.; Isola, C.; Laberinti, P.; Martimort, P. Sentinel-2: ESA's Optical High-Resolution Mission for GMES Operational Services. *Remote sensing of Environment* **2012**, *120*, 25–36.
8. Camps-Valls, G. Machine Learning in Remote Sensing Data Processing.; IEEE, 2009; pp. 1–6.
9. Lary, D.J.; Alavi, A.H.; Gandomi, A.H.; Walker, A.L. Machine Learning in Geosciences and Remote Sensing. *Geoscience Frontiers* **2016**, *7*, 3–10.

10. Maxwell, A.E.; Warner, T.A.; Fang, F. Implementation of Machine-Learning Classification in Remote Sensing: An Applied Review. *International Journal of Remote Sensing* **2018**, *39*, 2784–2817.
11. Thompson, D.; Brodrick, P. Making Machine Learning Work for Geoscience: Imaging Spectroscopy as a Case Example. *EOS* **2021**.
12. Roscher, R.; Bohn, B.; Duarte, M.; Garcke, J. Explain It to Me–Facing Remote Sensing Challenges in the Bio-and Geosciences With Explainable Machine Learning. *ISPRS Annals of the Photogrammetry, Remote Sensing and Spatial Information Sciences* **2020**, *3*, 817–824.
13. Small, C. Grand Challenges in Remote Sensing Image Analysis and Classification. *Frontiers in Remote Sensing* **2021**, *1*.
14. Cayton, L. Algorithms for Manifold Learning. *Univ. of California at San Diego Tech. Rep* **2005**, *12*, 1.
15. Izenman, A.J. Introduction to Manifold Learning. *WIREs Computational Statistics* **2012**, *4*, 439–446, doi:10.1002/wics.1222.
16. Van Der Maaten, L.; Postma, E.; Van den Herik, J. Dimensionality Reduction: A Comparative Review. *J Mach Learn Res* **2009**, *10*, 13.
17. Pearson, K. LIII. On Lines and Planes of Closest Fit to Systems of Points in Space. *null* **1901**, *2*, 559–572, doi:10.1080/14786440109462720.
18. Small, C. Spatiotemporal Dimensionality and Time-Space Characterization of Multitemporal Imagery. *Remote Sensing of Environment* **2012**, *124*, 793–809.
19. Woodcock, C.E.; Strahler, A.H. The Factor of Scale in Remote Sensing. *Remote Sensing of Environment* **1987**, *21*, 311–332, doi:10.1016/0034-4257(87)90015-0.
20. Adams, J.B.; Smith, M.O.; Johnson, P.E. Spectral Mixture Modeling: A New Analysis of Rock and Soil Types at the Viking Lander 1 Site. *Journal of Geophysical Research: Solid Earth* **1986**, *91*, 8098–8112, doi:10.1029/JB091iB08p08098.
21. Gillespie, A. Interpretation of Residual Images: Spectral Mixture Analysis of AVIRIS Images, Owens Valley, California. In Proceedings of the Proc. second airborne visible/infrared imaging spectrometer (AVIRIS) workshop; NASA: Pasadena, California, 1990; pp. 243–270.
22. Smith, M.O.; Ustin, S.L.; Adams, J.B.; Gillespie, A.R. Vegetation in Deserts: I. A Regional Measure of Abundance from Multispectral Images. *Remote Sensing of Environment* **1990**, *31*, 1–26, doi:10.1016/0034-4257(90)90074-V.
23. I. Niv; Y. Bregman; N. Rabin Identification of Mine Explosions Using Manifold Learning Techniques. *IEEE Transactions on Geoscience and Remote Sensing* **2022**, *60*, 1–13, doi:10.1109/TGRS.2022.3153520.
24. Li, H.; Cui, J.; Zhang, X.; Han, Y.; Cao, L. Dimensionality Reduction and Classification of Hyperspectral Remote Sensing Image Feature Extraction. *Remote Sensing* **2022**, *14*, 4579, doi:10.3390/rs14184579.
25. Sobien, D.; Higgins, E.; Krometis, J.; Kauffman, J.; Freeman, L. Improving Deep Learning for Maritime Remote Sensing through Data Augmentation and Latent Space. *Machine Learning and Knowledge Extraction* **2022**, *4*, 665–687, doi:10.3390/make4030031.
26. Liu, Y.; Chen, J.; Tan, C.; Zhan, J.; Song, S.; Xu, W.; Yan, J.; Zhang, Y.; Zhao, M.; Wang, Q. Intelligent Scanning for Optimal Rock Discontinuity Sets Considering Multiple Parameters Based on Manifold Learning Combined with UAV Photogrammetry. *Engineering Geology* **2022**, *309*, 106851, doi:10.1016/j.enggeo.2022.106851.
27. Sousa, F.J.; Sousa, D.J. Hyperspectral Reconnaissance: Joint Characterization of the Spectral Mixture Residual Delineates Geologic Unit Boundaries in the White Mountains, CA. *Remote Sensing* **2022**, *14*, doi:10.3390/rs14194914.
28. Sousa, D.; Small, C. Joint Characterization of Multiscale Information in High Dimensional Data. *Advances in Artificial Intelligence and Machine Learning* **2021**, *1*, 196–212, doi:10.54364/AAIML.2021.1113.
29. Small, C.; Sousa, D. Joint Characterization of the Cryospheric Spectral Feature Space. *Frontiers in Remote Sensing* **2021**, *2*.
30. Sousa, D.; Small, C. Joint Characterization of Spatiotemporal Data Manifolds. *Frontiers in Remote Sensing* **2022**, *3*, 760650, doi:10.3389/frsen.2022.760650.
31. Small, C.; Sousa, D. The Climatic Temporal Feature Space: Continuous and Discrete. *Advances in Artificial Intelligence and Machine Learning* **2021**, *1*, 165–183.
32. Small, C.; Sousa, D. The Sentinel 2 MSI Spectral Mixing Space. *Remote Sensing* **2022**.

33. McInnes, L.; Healy, J.; Melville, J. Umap: Uniform Manifold Approximation and Projection for Dimension Reduction. *arXiv preprint arXiv:1802.03426* **2018**.
34. Mitchell, T.D.; Jones, P.D. An Improved Method of Constructing a Database of Monthly Climate Observations and Associated High-resolution Grids. *International Journal of Climatology: A Journal of the Royal Meteorological Society* **2005**, *25*, 693–712.
35. Houghton, E. *Climate Change 1995: The Science of Climate Change: Contribution of Working Group I to the Second Assessment Report of the Intergovernmental Panel on Climate Change*; Cambridge University Press, 1996; Vol. 2; ISBN 0-521-56436-0.
36. Small, C. The Landsat ETM+ Spectral Mixing Space. *Remote Sensing of Environment* **2004**, *93*, 1–17, doi:10.1016/j.rse.2004.06.007.
37. Small, C.; Milesi, C. Multi-Scale Standardized Spectral Mixture Models. *Remote Sensing of Environment* **2013**, *136*, 442–454, doi:10.1016/j.rse.2013.05.024.
38. Sousa, D.; Small, C. Global Cross-Calibration of Landsat Spectral Mixture Models. *Remote Sensing of Environment* **2017**, *192*, 139–149, doi:10.1016/j.rse.2017.01.033.
39. Sousa, D.; Small, C. Globally Standardized MODIS Spectral Mixture Models. *Remote Sensing Letters* **2019**, *10*, 1018–1027, doi:10.1080/2150704X.2019.1634299.
40. Sousa, D.; Small, C. Multisensor Analysis of Spectral Dimensionality and Soil Diversity in the Great Central Valley of California. *Sensors* **2018**, *18*, 583, doi:10.3390/s18020583.
41. Sousa, D.; Brodrick, P.G.; Cawse-Nicholson, K.; Fisher, J.B.; Pavlick, R.; Small, C.; Thompson, D.R. The Spectral Mixture Residual: A Source of Low-Variance Information to Enhance the Explainability and Accuracy of Surface Biology and Geology Retrievals. *Journal of Geophysical Research: Biogeosciences* **2022**, *127*, e2021JG006672, doi:https://doi.org/10.1029/2021JG006672.
42. Settle, J.J.; Drake, N.A. Linear Mixing and the Estimation of Ground Cover Proportions. *International Journal of Remote Sensing* **1993**, *14*, 1159–1177, doi:10.1080/01431169308904402.
43. Kauth, R.J.; Thomas, G.S. The Tasselled Cap -- A Graphic Description of the Spectral-Temporal Development of Agricultural Crops as Seen by LANDSAT. In Proceedings of the Symposium on Machine Processing of Remotely Sensed Data; The Laboratory for Applications of Remote Sensing, Purdue University: West Lafayette, Indiana, 4B, July 29 1976; Vol. Paper 159, pp. 41–51.
44. Crist, E.P.; Cicone, R.C. A Physically-Based Transformation of Thematic Mapper Data—The TM Tasseled Cap. *IEEE Transactions on Geoscience and Remote Sensing* **1984**, *GE-22*, 256–263, doi:10.1109/TGRS.1984.350619.
45. McInnes, L. UMAP: Uniform Manifold Approximation and Projection for Dimension Reduction — Umap 0.5 Documentation Available online: https://umap-learn.readthedocs.io/en/latest/ (accessed on 13 October 2022).
46. Boardman, J.W. Automating Spectral Unmixing of AVIRIS Data Using Convex Geometry Concepts.; 1993; Vol. 1, pp. 11–14.
47. Boardman, J.W. Leveraging the High Dimensionality of AVIRIS Data for Improved Sub-Pixel Target Unmixing and Rejection of False Positives: Mixture Tuned Matched Filtering.; NASA Jet Propulsion Laboratory, 1998; Vol. 97, pp. 55–56.
48. Parker, R. *Geophysical Inverse Theory*; Princeton University Press, 1994; ISBN 978-0-691-03634-2.
49. Tarantola, A. *Inverse Problem Theory and Methods for Model Parameter Estimation*; SIAM, 2005; ISBN 0-89871-572-5.
50. Menke, W. *Geophysical Data Analysis: Discrete Inverse Theory*; 4th ed.; Academic Press: Cambridge, MA, 2018; ISBN 978-0-12-813556-3.
51. Bachmann, C.M.; Ainsworth, T.L.; Fusina, R.A. Exploiting Manifold Geometry in Hyperspectral Imagery. *IEEE Transactions on Geoscience and Remote Sensing* **2005**, *43*, 441–454, doi:10.1109/TGRS.2004.842292.
52. Gillis, D.; Bowles, J.; Lamela, G.M.; Rhea, W.J.; Bachmann, C.M.; Montes, M.; Ainsworth, T. Manifold Learning Techniques for the Analysis of Hyperspectral Ocean Data.; International Society for Optics and Photonics, 2005; Vol. 5806, pp. 342–351.
53. van der Maaten, L.; Hinton, G. Visualizing Data Using T-SNE. *Journal of machine learning research* **2008**, *9*, 2579–2605.
54. Belkin, M.; Niyogi, P. Laplacian Eigenmaps for Dimensionality Reduction and Data Representation. *Neural Computation* **2003**, *15*, 1373–1396, doi:10.1162/089976603321780317.

55. Kobak, D.; Linderman, G.C. Initialization Is Critical for Preserving Global Data Structure in Both T-SNE and UMAP. *Nature biotechnology* **2021**, *39*, 156–157.
56. Xiang, R.; Wang, W.; Yang, L.; Wang, S.; Xu, C.; Chen, X. A Comparison for Dimensionality Reduction Methods of Single-Cell RNA-Seq Data. *Frontiers in Genetics* **2021**, *12*.
57. Hozumi, Y.; Wang, R.; Yin, C.; Wei, G.-W. UMAP-Assisted K-Means Clustering of Large-Scale SARS-CoV-2 Mutation Datasets. *Computers in Biology and Medicine* **2021**, *131*, 104264, doi:10.1016/j.compbiomed.2021.104264.
58. Jiale, Y.; Ying, Z. Visualization Method of Sound Effect Retrieval Based on UMAP. In Proceedings of the 2020 IEEE 4th Information Technology, Networking, Electronic and Automation Control Conference (ITNEC); June 12 2020; Vol. 1, pp. 2216–2220.
59. Small, C. Multiresolution Analysis of Urban Reflectance.; IEEE, 2001; pp. 15–19.
60. Green, R.O.; Mahowald, N.; Ung, C.; Thompson, D.R.; Bator, L.; M. Bennet; M. Bernas; N. Blackway; C. Bradley; J. Cha; et al. The Earth Surface Mineral Dust Source Investigation: An Earth Science Imaging Spectroscopy Mission. In Proceedings of the 2020 IEEE Aerospace Conference; March 7 2020; pp. 1–15.
61. Krutz, D.; Müller, R.; Knodt, U.; Günther, B.; Walter, I.; Sebastian, I.; Säuberlich, T.; Reulke, R.; Carmona, E.; Eckardt, A.; et al. The Instrument Design of the DLR Earth Sensing Imaging Spectrometer (DESIS). *Sensors* **2019**, *19*, doi:10.3390/s19071622.
62. Candela, L.; Formaro, R.; Guarini, R.; Loizzo, R.; Longo, F.; Varacalli, G. The PRISMA Mission. In Proceedings of the 2016 IEEE International Geoscience and Remote Sensing Symposium (IGARSS); July 10 2016; pp. 253–256.
63. Nieke, J.; Rast, M. Towards the Copernicus Hyperspectral Imaging Mission for the Environment (CHIME).; IEEE, 2018; pp. 157–159.
64. Iwasaki, A.; Ohgi, N.; Tanii, J.; Kawashima, T.; Inada, H. Hyperspectral Imager Suite (HISUI)-Japanese Hyper-Multi Spectral Radiometer.; IEEE, 2011; pp. 1025–1028.
65. Thompson, D.R.; Schimel, D.S.; Poulter, B.; Brosnan, I.; Hook, S.J.; Green, R.O.; Glenn, N.; Guild, L.; Henn, C.; Cawse-Nicholson, K. NASA's Surface Biology and Geology Concept Study: Status and Next Steps.; IEEE, 2021; pp. 3269–3271.
66. Asner, G.P.; Knapp, D.E.; Boardman, J.; Green, R.O.; Kennedy-Bowdoin, T.; Eastwood, M.; Martin, R.E.; Anderson, C.; Field, C.B. Carnegie Airborne Observatory-2: Increasing Science Data Dimensionality via High-Fidelity Multi-Sensor Fusion. *Remote Sensing of Environment* **2012**, *124*, 454–465, doi:10.1016/j.rse.2012.06.012.
67. Boardman, J.W.; Green, R.O. Exploring the Spectral Variability of the Earth as Measured by AVIRIS in 1999. In Proceedings of the Summaries of the 8th Annu. JPL Airborne Geosci. Workshop; NASA: Pasadena, California, 2000; Vol. 1, pp. 1–12.
68. Cawse-Nicholson, K.; Hook, S.J.; Miller, C.E.; Thompson, D.R. Intrinsic Dimensionality in Combined Visible to Thermal Infrared Imagery. *IEEE Journal of Selected Topics in Applied Earth Observations and Remote Sensing* **2019**, *12*, 4977–4984, doi:10.1109/JSTARS.2019.2938883.
69. Cawse-Nicholson, K.; Damelin, S.B.; Robin, A.; Sears, M. Determining the Intrinsic Dimension of a Hyperspectral Image Using Random Matrix Theory. *IEEE Transactions on Image Processing* **2013**, *22*, 1301–1310, doi:10.1109/TIP.2012.2227765.
70. Thompson, D.R.; Boardman, J.W.; Eastwood, M.L.; Green, R.O. A Large Airborne Survey of Earth's Visible-Infrared Spectral Dimensionality. *Opt. Express* **2017**, *25*, 9186–9195, doi:10.1364/OE.25.009186.
71. Tenenbaum, J.B.; Silva, V. de; Langford, J.C. A Global Geometric Framework for Nonlinear Dimensionality Reduction. *Science* **2000**, *290*, 2319, doi:10.1126/science.290.5500.2319.
72. Kruskal, J.B. Multidimensional Scaling by Optimizing Goodness of Fit to a Nonmetric Hypothesis. *Psychometrika* **1964**, *29*, 1–27, doi:10.1007/BF02289565.
73. Kruskal, J.B. Nonmetric Multidimensional Scaling: A Numerical Method. *Psychometrika* **1964**, *29*, 115–129, doi:10.1007/BF02289694.